VIBRATIONAL DYNAMICS OF ICY AEROSOL PARTICLES: PHASE TRANSITIONS AND INTRINSIC PARTICLE PROPERTIES

by

Omar Freyr Sigurbjornsson
B.Sc., The University of Iceland, 2006

A THESIS SUBMITTED IN PARTIAL FULFILLMENT OF
THE REQUIREMENTS FOR THE DEGREE OF

MASTER OF SCIENCE

in

THE FACULTY OF GRADUATE STUDIES
(CHEMISTRY)

THE UNIVERSITY OF BRITISH COLUMBIA
(Vancouver)
November 2008

ABSTRACT

Phase transitions and other intrinsic properties (shape, size, architecture) of molecularly structured aerosol particles are important for understanding their role in planetary atmospheres and for technical applications. By combining bath gas cooling with time resolved mid-infrared spectroscopy and modeling, information is obtained on dynamic processes and intrinsic properties of fluoroform and ethane aerosol particles.

The distinct infrared spectral features of fluoroform aerosol particles make it a particularly suitable model system. Homogeneous crystallization rates of the sub-micron sized aerosol particles are determined ($J_V = 10^8$ - 10^{10} $cm^{-3}s^{-1}$ or $J_S = 10^3 – 10^5$ $cm^{-2}s^{-1}$ at a temperature of T = 78 K), and the controversial question regarding volume versus surface nucleation in freezing aerosols is addressed. It is demonstrated that current state of the art measurements of droplet ensembles cannot distinguish between the two mechanisms due to inherent experimental uncertainties. The evolution of particle shape from spherical supercooled droplets to cube-like crystalline particles and eventually to elongated crystalline particles is recorded and analyzed in detail with the help of vibrational exciton model calculations.

Phase behaviour of pure ethane aerosols and ethane aerosols formed in the presence of other ice nuclei under conditions mimicking Titan's atmosphere provide evidence for the formation of supercooled liquid ethane aerosol droplets, which subsequently crystallize. The observed homogeneous freezing rates ($J_V = 10^7 – 10^9$ $cm^{-3}s^{-1}$) imply that supercooled ethane could play a similar role in ethane rich regions of Titan's atmosphere as supercooled water does in the Earth's atmosphere.

TABLE OF CONTENTS

LIST OF TABLES

LIST OF FIGURES

ACKNOWLEDGEMENTS

First and foremost I wish to thank my supervisor, Dr. Ruth Signorell for her enthusiasm and dedication, which has been the driving force of this research. I am thankful for the opportunity to work with her and grow in my own abilities to conduct independent research.

I would also like to thank all those people with whom I have had the privilege to work with over the past two years at UBC. I am greatly indebted to all members of the research group for their direct or indirect contribution to this project, Specifically; Stephan Jauer and Jennifer Johnson for their help with setting up the experiment, Simran Kular for her contributions to the measurements and data analysis, Piotr Forysinski, Philipp Zielke and Moritz Gadermann for all their help and expertise around the lab, Dr. David Luckhaus for writing the non-linear least squares fit program for the crystallization rate constants and Chia Wang, for helpful comments regarding the thesis manuscript. I am particularly grateful for the collaboration with George Firanescu and his efforts on the modeling side of this project. In addition to those already mentioned I also thank Thomas Preston, Angelina Weiss, Jennifer Leung and Ricardo Viteri for keeping spirits high around the office and making it an enjoyable place to conduct research. I value all your friendship and support.

Lastly I thank my extended family in Vancouver, Al & Linda Copland and the good people at St. John's college for making me feel at home in Vancouver during my stay.

DEDICATION

Tileinkað foreldrum mínum

(Dedicated to my parents)

CHAPTER 1

INTRODUCTION

1.1 General Introduction to Aerosols

The term ‘aerosol’ describes liquid droplets or solid particles of arbitrary shape that are suspended in a gaseous medium. They can be classified as a unique form of matter, having properties that are significantly different from those of gaseous molecules or bulk matter. Their size range extends over several orders of magnitude, from sub-nanometer aggregates to particles hundreds of micrometers in size.

Aerosols are important for understanding atmospheric processes on earth [1, 2], as well as in planetary atmospheres of the outer solar system [3, 4]. Various types of small particles and molecular aggregates are also present in the interstellar medium [5]. On earth, aerosols are ubiquitous in our environment, in such varying forms as smoke, mist, fog and smog. Their presence affects our climate by altering the properties of cloud and rain formation by acting as condensation nuclei. Through absorbing and scattering solar radiation, aerosols affect radiative transfer processes and thus the energy balance of the atmosphere [6]. Reactions that take place on grain surfaces play an important role in atmospheric and interstellar chemistry [7], but are in general poorly understood compared to gas phase reactions. The presence of aerosols in smog pollution can have adverse affects on health in urban areas [8]. In addition to the areas already mentioned, the knowledge of aerosol properties is of significant interest in technical processes [9], for example in the micronization of pharmaceuticals [10] for increased bioavailability.

1.2 Intrinsic Particle Properties from Infrared Spectra

The wide ranging implications of aerosols (as stated in the previous section) have led to a significant amount of interest in their properties. Their finite-size gives rise to unique properties, which can be drastically different from the bulk. However, the molecular origins of those properties are in many cases poorly understood. This challenge comes as a result of the large number of degrees of freedom within these systems. To resolve these issues, improvements in both theoretical and experimental investigations need to go hand in hand.

Molecularly structured aerosol particles are held together by weak intermolecular forces (hydrogen bonds, van der Waals forces). For a theoretical treatment of large systems, it becomes necessary to make approximations in order to come up with models that still capture the essential features of molecular interactions in aerosols, but are simple enough to be computationally feasible. Experimentally, the challenges lie in generating well defined particle ensembles and studying the system non-intrusively under relevant conditions. An important point is, for example, that the particles are studied in the aerosol phase and not on substrates, in order to avoid interactions with the latter. For the phase transitions discussed in the present thesis it is also crucial that the particles are in thermal equilibrium with the surrounding gas phase.

Various spectroscopic techniques have been adapted to the study of aerosol particles [11, 12]. These can be used to address fundamental questions about their intrinsic properties, such as size, shape and internal structure [13-17] . To answer those questions it is necessary to understand how they manifest themselves in the spectra. This requires modeling of the interaction of light with the particles, either in a classical way,

or by employing a molecular approach. The methods and approximations chosen depend on the nature of the system and the properties of interest.

The emphasis in this thesis is to demonstrate how intrinsic particle properties can be extracted from mid-infrared extinction spectra of molecularly structured aerosol particles. Infrared spectroscopy is particularly suitable for molecularly structured aerosol, since it provides a wealth of information on these systems. In many cases, the vibrational dynamics can be used to probe the local structure of molecules in a particle, as well as the overall structure of small (sub-micrometer sized) particles.

It has been shown that it is possible to obtain specific information about intrinsic particle properties (size, shape, architecture, internal structure) for a large number of particle systems, using a simple yet effective model (section 3.1.2). Specifically, the influence of particle size, shape, architecture and internal structure on the infrared absorption bands can be identified and distinguished from one another. Such characteristic features can in turn influence other properties such as the phase behaviour, the chemical reactivity and in the case of drug particles even their bioavailability. The ability to discern those details is extremely valuable for characterization of atmospheric aerosols and interstellar ice particles (discussed in section 1.4), as well as for drug particles.

In general, it has been found that particles in the size range between 10-100 nm usually do not display size dependent features in mid-infrared spectra (apart from a trivial scaling of the absorbance), whereas larger particles exhibit signs of elastic light scattering. Spectra of particles smaller than 10 nm are strongly size dependent. This is mainly due to effects from increased number of molecules at the surface compared to the

volume of the particles. Whether or not shape effects are present in the spectra depends on the strength of the resonant molecular transition dipole coupling (present for transition dipoles > 0.1-0.2 D) and distances between neighbouring molecules within the particle (distances < 5-7 Å) [14].

1.3 Phase Transitions in Particles - Surface vs. Volume Nucleation

Phase transitions in aerosol particles are important for physical processes in earth's and other planetary atmospheres [18]. A fundamental question about their phase behaviour relates to the mechanism of homogeneous crystallization in supercooled droplets. Under conditions free of appreciable amounts of crystallization nuclei (that can induce heterogeneous crystallization), atmospheric aerosol droplets (for example water droplets in the Earth's atmosphere) can exist in a highly supercooled state [19]. Given deep enough supercooling, the aerosol droplets will eventually crystallize homogeneously. Despite extensive investigations this remains a topic of debate and continued research efforts. The initial and still the most widely employed theoretical formulation of this process is Classical Nucleation Theory (CNT), presented briefly in section 3.2. An inherent assumption for particulate systems is that nucleation takes place within the volume of a particle, while in principle this could also happen at the surface. By the re-analysis of experimental data [20-23] and thermodynamic arguments [24] it has been claimed that surface nucleation might dominate as the crystallization mechanism in atmospherically relevant aerosol droplets, with possible significant implications for modeling and understanding of atmospheric processes.

Homogeneous crystallization according to classical nucleation theory is a stochastic process based on the formation of critical nuclei from random thermal motion. As such the rates of surface and volume nucleation will depend on the relative number of molecules involved. In large particles (larger than a few micrometers) the number of molecules at the surface is insignificant compared to those within its volume. Surface nucleation is therefore not likely to have a dominating effect. Conversely, in particles smaller than a few nanometers almost all molecules reside at or near the surface and therefore surface nucleation is likely to dominate. It is in this crucial size range, between a few nanometers to a few micrometres, where investigations need to take place.

A critical review of previous investigations is presented in sections 4.3.4, as well as improvements to the kinetic treatment of ensemble measurements in section 3.2. The latter are then implemented in the study of fluoroform aerosol crystallization, as a model system to address the important question of whether surface or volume nucleation dominates in freezing aerosols [25].

1.4 Aerosol Particles in Planetary Atmospheres and on Titan

In the study of planetary atmospheres and the interstellar medium, aerosols are often referred to as haze or haze particles but also as grains, dust and particulates. Micron-sized dust grains comprise roughly 1 % of the mass of the interstellar medium [5]. Grain surface reactions are needed to account for the formation of a number of interstellar molecules [7], although the process is much less understood than gas phase reaction pathways.

Aerosols are likely to be present in the atmospheres of all the giant planets in the outer solar system [3, 26-29] as well as on Saturn's moon, Titan [30-32]. There is evidence for icy ammonia aerosol clouds on Jupiter [33] and Saturn [34], and condensed simple hydrocarbons (CH_4, C_2H_2 and C_2H_6) on Uranus [35], Neptune[4] and Titan. In addition, Titan is shrouded by optically thick haze layers formed from complex organic molecules.

Planetary aerosols are significant for several reasons. As on earth, aerosols affect radiative transfer processes and thus the atmospheric energy balance through scattering of light. These scattering haze or cloud layers can partially (or fully) obscure the lower parts of the atmosphere as well as their surface, and cause anti-greenhouse effects, where the lower atmosphere gets cooled while the upper atmosphere is heated. Aerosols can also potentially be used as tracers of atmospheric conditions and the dynamic processes taking place.

Investigations of planetary atmospheres rely primarily on remote sensing through UV, visible and infrared spectroscopy of scattered solar radiation and thermal emission [36]. These data are mainly obtained from ground based or orbiting telescopes. Space

mission orbiters and probes such as Voyager, Pioneer, Galileo and most recently Cassini-Huygens, are another crucial source of valuable information. In-situ measurements of aerosol particles have been performed on Titan with the Huygens probe [37, 38] and on Jupiter with the Galileo probe [39]. To understand the data obtained from these various sources of observations, laboratory studies are needed, which simulate the relevant conditions. In particular, spectroscopic characterization of icy aerosol particles is required for their remote detection. As discussed in section 1.2 and later chapters, spectroscopy can also provide valuable information about the structure and dynamic properties of the particles.

Recent investigations of Titan's atmosphere, particularly by the Cassini-Huygens space mission, have revealed a fascinating environment where aerosols play an important role. In order to understand the importance and implications of aerosols in Titan's atmosphere it becomes necessary to know more about the conditions on this unique moon. Historically, the primary interest in Titan has been due to its dense atmosphere (a pressure of 1.5 bar at the surface) that consists of mainly nitrogen (95-98%) and methane (1.5-4 %) [40, 41], as well as the haze layers that obscure the surface of the moon. More recently a cycle of evaporation, condensation and precipitation of methane and ethane has been discovered, analogous to the hydrological cycle on Earth. This is so far the only other body in the solar system where such processes are actively involved in shaping its surface. As a consequence, liquid reservoirs have been found on the surface [42]. The main difference between the atmospheres of Earth and Titan, however, lies in the temperature at which these processes take place and the compounds involved. The temperature minimum in Titan's atmosphere of 70 K is reached at an altitude of 50 km

above the surface (the tropopause), which has a temperature of 93.7 K. As a comparison, temperatures at Earth's tropopause lie around 217 K.

Photochemical reactions of N_2 and CH_4 higher up in Titan's atmosphere are responsible for forming larger molecules such as C_2H_2, C_2H_6 and HCN [43] which, when transported down to lower altitudes and temperatures, condense into particles. These particles are then expected to act as nucleation sites for CH_4 condensation. So far, however, there exists no conclusive proof for the presence of methane aerosols on Titan [44]. On the contrary, there exists strong evidence for ethane clouds [32]. Ethane aerosols are the focus of the present thesis.

These photochemical reactions also lead to the formation of a complex polymeric mixture of non-volatile organic compounds, commonly referred to as tholin particles [45, 46]. They form the haze layers in the stratosphere. Numerous experimental studies have focused on reproducing and characterizing these so-called Titan tholins in a laboratory setting [47, 48].

1.5 Thesis Overview

The material presented in this thesis is organized into 6 chapters as follows. This chapter discusses some of the fundamental aspects of aerosols, and outlines the challenging issues associated with them that are addressed in the following chapters. Chapter 2 accounts for the general experimental methods that were used for producing and studying the aerosol particles. In chapter 3, the theoretical framework for the interaction of infrared light with particles is given. Both the classical model and the vibrational exciton model are presented. The classical nucleation theory of homogeneous phase change is briefly summarized and extended to the treatment of the kinetics of particle ensemble measurements. Chapter 4 is devoted to the study of fluoroform aerosol as a model system, both to determine the influence of surface or volume nucleation on the freezing of sub-micron sized droplets, and to clarify how intrinsic particle properties manifest in infrared spectra. In chapter 5 ethane aerosol particles are studied in the context of their presence in Titan's atmosphere, and the possible phases and phase transitions under Titan's conditions are characterized. Chapter 6 summarizes the findings of the thesis and outlines the work that remains to be done on these topics. The work presented in this thesis has resulted in three publications [25, 49, 50] and has been covered in part in a review article [17].

CHAPTER 2

EXPERIMENTAL SECTION

2.1 Introduction

The generation and study of the aerosol particles reported in this thesis was achieved by using a custom built collisional cooling cell, described in chapter 2.2. The aerosols were formed by rapidly injecting a warm sample gas mixture into a pre-cooled bath gas. If the bath gas temperature is below the boiling point of the substance and the degree of supersaturation is sufficiently high, condensation and aerosol formation occurs. The aerosol formation process and subsequent time evolution was then monitored by recording the mid-infrared spectra *in situ*. Infrared spectroscopy is ideal for probing the dynamics, shapes and phases of molecularly structured, sub-micron sized particles. This is due to the fact that the frequencies and intensities of vibrations are sensitive not only to the local environment in the particles, but in some cases (strong transition dipole couplings) also to particle properties such as shape and size.

There are several advantages of using a collisional cooling cell in combination with infrared spectroscopy to study aerosol particles. Most importantly, measurements are performed on unsupported free particles in thermal equilibrium with their surroundings. Their time evolution can then be studied non-invasively and the combination with long optical pathlengths allows for high sensitivity. A more common laboratory generation of weakly bound molecular aggregates is by supersonic jet expansions [51] using nozzles of varying design (slit nozzles, Laval nozzles). In comparison, collisional cooling affords

much longer observation times (minutes to hours compared with milliseconds at best in supersonic expansions) and unlike supersonic expansions it allows measurements under thermal equilibrium over a wide range of temperatures (4-298 K) and a wide range of particles sizes (less than 1 nm to hundreds of micrometers). Thermal equilibrium between particles and surrounding gas phase and thus a well defined temperature are crucial for the study of phase transitions. In addition jet expansions can suffer from low signal intensity and require large amounts of sample gas.

Several previous studies on molecular aggregates using collisional cooling techniques exist in the literature, notably those by George Ewing [52], Roger Miller [53, 54] and Paul Devlin [55, 56]. However those studies often suffer from certain limitations caused by the design of their experiments. For example, small cell dimensions can cause effects from particles being adsorbed on the walls. Insufficient or inhomogeneous cooling can also lead to inaccuracies, especially when studying particle phase transitions. Our cell is particularly well suited for this purpose due to the large cell dimensions (8 L inner volume) and temperature control over a wide range, thus effectively eliminating wall effects and allowing for long observation times. Moreover, it is to our knowledge the only cooling cell coupled with a rapid-scan FTIR spectrometer, essential for high time resolution measurements (ms).

2.2 Experimental Setup

The experimental setup of the cooling cell is shown schematically in figure 2.1. It is similar to the one described in ref. [57] and has been reported previously [14, 58]. It consists of an outer vacuum cylinder which thermally isolates the inner parts of the cell. A stainless steel cylinder for cooling agent can be filled with liquid nitrogen or liquid helium, depending on the desired cell temperature. This provides cooling for the inner "cooling cell" that contains the helium bath gas (typically 0.1-1 bar pressure at 78 K) and optical mirrors. At low temperature and high vacuum conditions it is necessary to use indium metal as sealing material for the cell. For temperature monitoring NiCr-Ni thermocouples are positioned in the upper, middle and lower part of the cell as well as on the mirrors. Conversion from mV readings to K units are performed according to calibration values given in ref. [59]. The cell is equipped with *White Optics* [60] giving an adjustable optical pathlength from 4 optical passes (3 m) and increasing in intervals of 4 passes up to a maximum of 24 passes (16 m). This makes it possible to detect low particle concentrations of very small particles. The gold coated optical mirrors can be electrically heated in order to avoid any sample condensation on the mirrors.

Sample gas injection into the cell is controlled by a set of Bürkert magnetic solenoid valves triggered by the infrared spectrometer through an electric pulse generator. Sample gas mixtures were prepared on a mixing line that is connected to the sample inlet system. The sample gas was introduced to the mixing line in the millibar pressure range and subsequently diluted with several bar pressure of helium, forming a statistical mixture of the gases after some minutes. Information about gases and mixture concentrations used in this thesis can be found in Table 2.1. The amount of sample gas

introduced into the cell is then controlled by the bath gas pressure (0.1-1 bar) in the cell, the backing pressure of the sample gas (few hundreds of millibars higher than the cell) and the pulse time duration (normally 1s). The pressure differential drives the warm sample gas from the mixing line and gas reservoir into the cold cell. A dual inlet system allows for the introduction of two separate substances or gas mixtures into the cell with time delays of milliseconds up to minutes. This makes it possible to form particles with core-shell architecture and to study the effects of heterogeneous nucleation. The inner diameter of each inlet tube is 2 mm. They can be heated to prevent any particle formation prior to entering the cell.

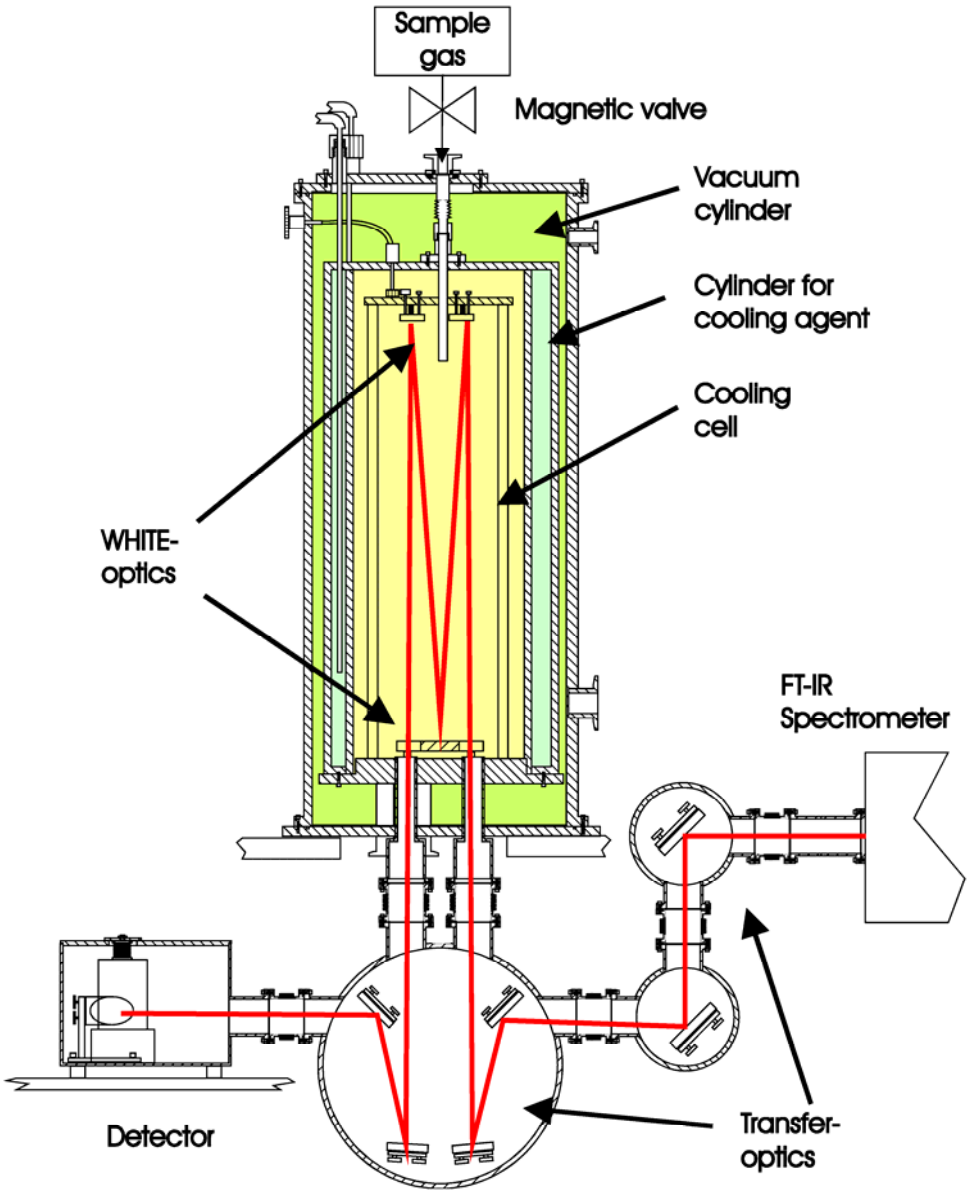

Figure 2.1 Schematic of the collisional cooling cell and transfer optics [14].

2.3 FTIR Spectroscopy *in situ*

The monitoring of particle formation, growth and phase change is made possible through *in situ* (i.e. in the aerosol phase while the processes are taking place) infrared measurements. The infrared extinction spectra were recorded using a rapid scan Bruker IFS66v/S Fourier transform infrared spectrometer (FTIR). The infrared beam is coupled into the cell and out to a mercury cadmium telluride (MCT) detector through evacuated transfer optics, separated from the cell using KBr windows. The set spectral resolution varied from 2 to 0.5 cm^{-1}. At spectral resolution of 2 cm^{-1} the spectrometer has a time resolution of 30 ms, making it possible to follow phase transitions and particle growth in detail. All spectra were recorded as absorption spectra ($A = -\log_{10}\frac{I}{I_0}$), using a mid-infrared globar light source and a KBr beamsplitter. Absorbance values varied typically between 0.001 and 1 with absorbance values above 1.2 considered saturated. The spectral range covered was normally from 500 cm^{-1} to 8000 cm^{-1}. The recording and subsequent handling of the spectra was done with the commercial spectroscopic software, OPUS. Typically 5-20 spectra were summed to improve the signal-to-noise ratio.

2.4 Materials and Experimental Conditions

An overview of the substances and mixture concentrations used for the investigations in this thesis is listed in Table 2.1. Typical experimental conditions consisted of bath gas pressures ranging from 100 to 1000 mbar, thermally equilibrated with the pre-cooled cell (78K) after some minutes. The bath gas used was commercially available helium (99.995%, Praxair) that was further dried before use by passing it through liquid nitrogen cooling traps in order to minimize trace water impurities.

Important for understanding and predicting the condensation and phase behaviour of substances are their vapour pressures as a function of temperature. The lower the vapour pressure is for a substance at a given temperature, the more likely it is that this substance condenses. The data shown in Figure 2.2 is for the four substances which are important in this thesis. Acetylene and CO_2 have low vapour pressures at temperatures below 150 K and can therefore condense and form (solid) particles more easily than fluoroform and ethane. This makes them suitable to act as condensation nuclei for substances such as fluoroform and ethane, and thus to study heterogeneous nucleation processes. The heterogeneous nucleation of fluoroform and ethane is discussed in sections 4.4.2 and 5.4, respectively.

Table 2.1 Overview of gases and their concentrations used in the experiments.

Substance	Supplier	Purity	Sample mixture concentration	Mole fraction in cell
Helium	Praxair	99.999 %	0 – 99.97 %	0.99 – 0.999999
Fluoroform	Spectragases	99.995 %	300 ppm – 5 %	10^{-6} – 10^{-3}
Ethane	Praxair	99.999 %	1000 ppm – 10 %	10^{-5} – 10^{-3}
Acetylene	Praxair	99.6 %	1000 ppm – 50 %	10^{-5} – 10^{-2}
Carbon dioxide	Praxair	99.998 %	2500 ppm – 100 %	10^{-5} – 10^{-2}

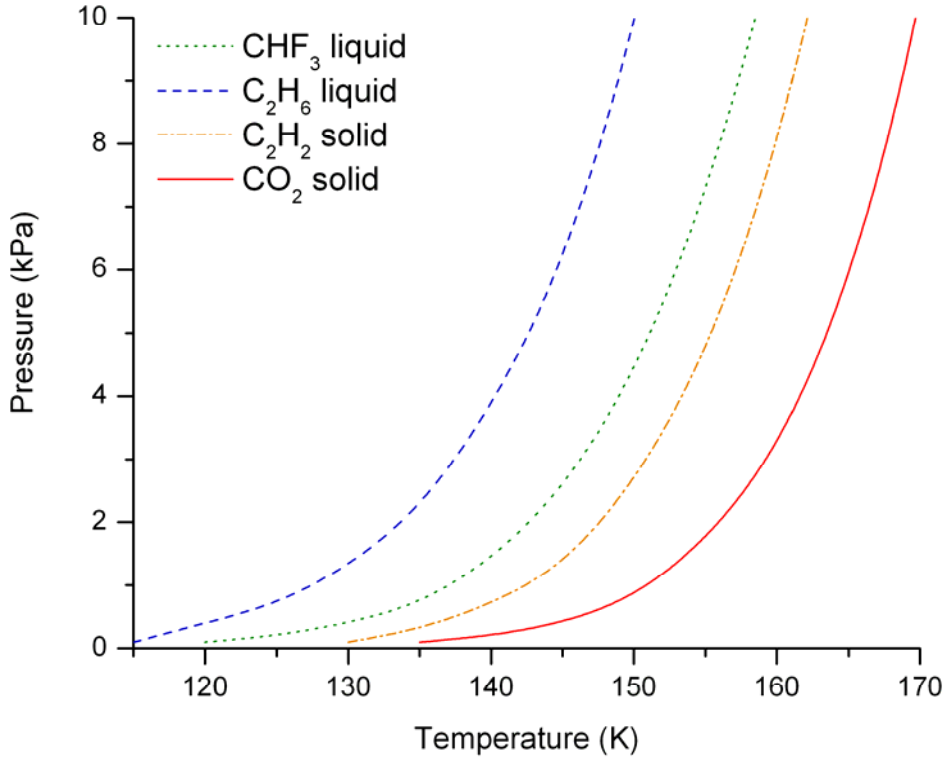

Figure 2.2 Vapour pressure as a function of temperature for the substances listed in table 2.1. Values are from CRC Handbook of Chemistry and Physics 88th ed.

CHAPTER 3

THEORY

3.1 Extinction of Light by Aerosol Particles

The interaction of electromagnetic (EM) waves with particulate matter gives rise to light extinction, strongly depending on the relative size of the particles and the wavelength of the light. Extinction is the attenuation of incident light by absorption and scattering as it passes through a medium, in our case an aerosol (for a collinear arrangement of the light source, the sample, and the detector). For molecularly structured aerosols, absorption is a dominant contribution to the extinction for particles of all sizes, shapes, and architectures. Elastic scattering, by contrast, is only important when the particle size is comparable to the wavelength of the light. In our studies we focus on the mid-infrared region (400 - 4000 cm^{-1}) where this applies to particles with radii above roughly 100 nm. Elastic scattering leads to slanted baselines and dispersion shapes of absorption bands in infrared extinction spectra. Classical scattering theory, such as Mie theory, can in principle be used to simulate extinction spectra, for example to estimate aerosol particle sizes (see section 3.1.1).

Classical scattering theory, however, does not provide any information on the molecular origins of extinction features and so a quantum mechanical model that takes into account the intermolecular and intramolecular interactions is required. While this can easily be done for small molecular clusters (up to several molecules per cluster) with standard quantum chemical program packages [28], the treatment of large molecular

aggregates containing hundreds to billions of molecules per particle is still unfeasible. It is therefore necessary to restrict the treatment to those intramolecular and intermolecular interactions that really dominate the vibrational structure. Adaptations of this kind have been put forth by several researchers to simulate vibrational spectra of medium sized molecular aggregates of water, ammonia, and carbon dioxide [52, 61-63]. These approaches are, however, limited to the treatment of sub-nanometer (some tens of molecules) to a few nanometers (some hundreds of molecules) molecular aggregates. This is not large enough to simulate the influence of intrinsic particle properties on the infrared absorption bands of aerosol particles with sizes in the sub-micrometer range (thousands to billions of molecules). To achieve this goal the Vibrational Exciton Model (discussed in chapter 3.1.2) is used. It is a simplified quantum mechanical model that takes into account as a major contribution the resonant transition dipole couplings and has previously been shown [14, 64] to capture the dominant effects in the vibrational structure of bands with strong transition dipoles (μ >0.1-0.2 D). By combining these two complimentary methods, information on molecularly structured aerosol particles can be obtained over a vast size domain (over four orders of magnitude).

3.1.1 Classical Scattering Theory/Mie Theory

Classical scattering theory can be used to calculate infrared extinction spectra, provided the refractive index data are available as input data. The scattering of light is defined as the redirection of electromagnetic waves through their interactions with matter. Oscillating electromagnetic fields can produce periodic charge separation in molecules or aerosol particles and thus induce in them a dipole moment. The oscillating dipoles are then the source of the scattered radiation. Relations between electric and magnetic fields and electric charges and currents are described by Maxwell's equations [65]. By solving those equations with boundary conditions for a certain particle-light system one can calculate extinction spectra. This is known as classical scattering theory [66, 67].

Classical scattering theory is a continuum theory that does not take into account the molecular structure of aerosol particles. It requires knowledge of the optical properties of the particle and the surroundings, namely the wavelength dependent complex index of refraction given by $N(\nu) = n(\nu) + ik(\nu)$ where n is the real part and k is the imaginary part. Two special cases of classical scattering theory are Rayleigh and Mie scattering. Mie theory applies to spherical aerosol particles. In order for Rayleigh scattering to apply the particle must be much smaller (the upper limit is roughly 1/10 the wavelength) in diameter than the wavelength of the scattered light. In Mie scattering calculations there is no such criteria as it is a complete analytical solution of Maxwell's equations for the scattering of EM waves by spherical particles in a homogeneous medium, valid for all possible ratios of diameter to wavelength. At large sizes it converges to the limit of geometric optics.

For a spherical particle, expressions for the scattered electric (E_s) and magnetic (H_s) fields are given in equations 3.1 and 3.2 as expansions of infinite series of vector spherical harmonics. Further details can be found in ref. [66, 68].

$$\vec{E}_s = E_0 \sum_{n=1}^{\infty} i^n \frac{2n+1}{n(n+1)} (ia_n \vec{N}_{e1n}^{(3)} - b_n \vec{M}_{o1n}^{(3)}) \tag{3.1}$$

$$\vec{H}_s = \frac{1}{i\omega\mu} \vec{\nabla} \times \vec{E}_s \tag{3.2}$$

Here E_0 is the amplitude of the incident electric field, ω is the frequency and μ is the permeability of the surrounding. $\vec{N}_{o1n}^{(3)}$ and $\vec{M}_{o1n}^{(3)}$ are vector spherical harmonics of the third kind (outgoing wave functions). The subscripts denote the symmetry of the spherical harmonic (even, e, or odd, o) and the order and degree of the associated Legendre functions and spherical Bessel functions, describing the angular variation of the EM field.

The coefficients a_n and b_n are defined in terms of spherical Bessel functions and spherical Hankel functions and depend on the particle radius, the complex refractive index and wavelength [66]. After obtaining the coefficients, we can calculate the extinction cross sections:

$$C_{ext} = \frac{2\pi}{\chi^2} \sum_{n=1}^{\infty} (2n+1) \operatorname{Re}[a_n + b_n] \tag{3.3}$$

$$C_{sca} = \frac{2\pi}{\chi^2} \sum_{n=1}^{\infty} (2n+1) \left[|a_n|^2 + |b_n|^2 \right] \tag{3.4}$$

$$\chi = \frac{2\pi \cdot N}{\lambda} \tag{3.5}$$

where N is the refractive index of the surroundings. The absorption cross section is then calculated from Equations 3.3 and 3.4:

$$C_{abs} = C_{ext} - C_{scat} \tag{3.6}$$

The total extinction can then be calculated by summing over different particle sizes as follows:

$$-\log_{10}\left(\frac{I}{I_0}\right) = \sum_j N_j C_{ext,j} l \tag{3.7}$$

where N_j is the number of particles of size j and l is the optical path length.

A major drawback to Mie theory calculations is the need for accurate complex index of refraction data [17]. These data are often unavailable or inaccurate. Even for pure aerosol particles the applicability is questionable as they are most often derived from thin film measurements under entirely different experimental conditions. All Mie calculations reported in this thesis were performed using a modified FORTRAN code given by Bohren and Huffman [66].

Several methods have been developed to solve Maxwell's equations for the scattering of light by particles of arbitrary size and shape. One of the more widely used methods is the Discrete Dipole Approximation (DDA) [69, 70]. It simulates light scattering by arbitrarily shaped particles by replacing the scatterer with a set of point dipoles. Another popular computational scheme is the finite-difference time-domain (FDTD) method [71].

3.1.2 Vibrational Exciton Model

To go beyond the treatment of classical scattering theory we employ a simplified quantum mechanical model called the Vibrational Exciton Model. It accounts for light absorption by molecularly structured aerosol particles, when transitional dipole coupling is the dominant interaction (molecular transition dipole μ>0.1-0.2 D) [15, 17, 64, 72]). A description for crystalline bulk systems was originally put forth by Hexter [73, 74] and later adapted to treat small finite sized particles [52, 63]. This coupling lifts the degeneracy of the uncoupled vibrational states of individual molecules. This gives rise to collective modes that are delocalized over the entire particle, which sensitively depend on the particle size, shape and architecture. They can therefore act as a probe for those intrinsic particle properties.

The vibrational Hamiltonian (including dipole coupling as well as polarization effects) can be written as:

$$\hat{H} = \hat{H}_0 + \sum_{i,j} \mu_i^+ A_{ij} \mu_j \qquad 3.7$$

Where $\hat{H}_0$ is the Hamiltonian for uncoupled molecular oscillators, μ_i is the dipole moment of molecule *i*. The sum extends over pairs of molecules i, j with:

$$A_{ij} = -\frac{1}{2}\left(\lambda_{ij} + \sum_k \lambda_{ik} \alpha_k \lambda_{jk} \right) \qquad 3.8$$

α_k is the polarizability tensor of molecule *k* and λ_{ij} are scaled projection matrices given by:

$$\lambda_{ij} = \frac{\left(1 - \delta_{ij}\right)}{4\pi\varepsilon_0 R_{ij}^3} \left(3 e_{ij} e_{ij}^+ - 1 \right) \qquad 3.9$$

where e_{ij} is the unit vector pointing from the center of mass of molecule i to that of molecule j and R_{ij} is the corresponding distance. Within the double harmonic approximation the Hamiltonian is completely defined by transition wavenumbers $\tilde{\nu}_{im}$, transition moments $\mu_{im} = \langle 0 | \mu_i | i_m \rangle$ and polarizability tensors α_i. $|im\rangle$ is the m-th eigenfunction of the i-th molecular oscillator. The calculated spectrum can then be obtained by diagonalizing the Hamilton matrix with matrix elements of the form:

$$\langle i_m | \hat{H} | j_n \rangle = \delta_{ij}\delta_{mn} hc\, \tilde{\nu}_{im} + 2\mu_{im}^{+} A_{ij} \mu_{jn} \qquad 3.10$$

Aerosol particles can however easily consist of tens of thousands of molecules and therefore tens of thousands of oscillators, for which full diagonalization of the Hamiltonian is no longer viable. In this case a time dependent approach can be taken to calculate absorption spectra directly from the dipole autocorrelation function.

$$C(t) = g(t) \sum_{k,m,l,n} \langle k_m | \mu_{km} e^{-i\hat{H}t/\hbar} \mu_{ln} | l_n \rangle \qquad 3.11$$

where $g(t)$ is the Fourier transform of a suitable window function $f(E)$. The correlation function $C(t)$ is calculated using a 2nd order propagation scheme:

$$|\psi_{t+\Delta t}\rangle = e^{-i\hat{H}\Delta t/\hbar} |\psi_t\rangle \approx -i\frac{2\Delta t}{\hbar}\hat{H}|\psi_t\rangle + |\psi_{t-\Delta t}\rangle \qquad 3.12$$

The resolution of the calculated infrared spectrum $\sigma(E)$ is then determined by the length of the time propagation step Δt.

As an added benefit to this theoretical treatment, it becomes possible to analyze particle IR spectra based on calculated spectral pseudo-density, first introduced in reference [15]. It is obtained by partitioning the spectrum $\sigma(E)$ into contributions $\sigma_i(E)$ from individual volume elements δV_i:

$$\sigma(E) = \sum_i \sigma_i(E) = \sum_i \int g(t) \sum_{k \in \delta V} \sum_{m,l,n} \langle k_m | \mu_{km} e^{-i\hat{H}t/\hbar} \mu_{ln} | l_n \rangle dt \qquad 3.13$$

where $\sigma_i(E)$ are obtained from an equivalent partitioning of $C(t)$ (Equation 3.11). For direct comparison between contributions from volume elements of different size, normalized excitation density is used:

$$\bar{\sigma}(E) = \sum_i \frac{\sigma_i(E)}{N_i} \qquad 3.14$$

where N_i is the number of molecules in δV_i. The origins of spectral features can then be mapped out (as shown in Figure 4.8) as a function of the particle radius allowing surface and core contributions to be identified.

All exciton model calculations presented in this thesis were performed by or in collaboration with George Firanescu, using FORTRAN code written and maintained by him.

3.2 Classical Nucleation Theory

Processes involving condensation of vapour and crystallization of liquids are ubiquitous in our surroundings and are of widespread interest in a number of disciplines such as chemistry, physics, materials and atmospheric sciences. In an attempt to describe these processes Classical Nucleation Theory (CNT) was first developed almost a century ago by Volmer and Weber [75] and later extended by Farkas [76], Becker and Döring [77] and Turnbull and Fisher [78]. No attempt is made to cover this extensive topic in detail here but the reader is referred to the texts of Kelton [79], Kashchiev [80] and Schmelzer [81] for a more general overview.

According to CNT, condensation and crystallization rates are determined by the rate of formation of critically sized nuclei (clusters bound by intermolecular forces) within the primary phase that subsequently grow until a phase change has occurred. The sizes of the clusters are Boltzmann distributed with temperature and the critical size depends on the energy of formation of a cluster. Energy of formation is determined by surface and volume energies and increases to a maximum which corresponds to the critical size. It is assumed that cluster size changes only by the addition and loss of monomer units and the formation of a critical nucleus is the rate limiting factor for the phase transition and not its subsequent growth. Several other approximations are made that relate bulk properties such as surface tension to the emerging nuclei. When the number and in some cases the crudeness of approximations is considered it is not surprising that this often leads to shortcomings when predicting nucleation rates. However due to its relatively simple use, wide range of application and a lack of a better approach CNT remains widely used.

Central points discussed in chapters 4 and 5 are the kinetics of homogeneous crystallization of aerosol particles [25]. The following discussion is therefore restricted to that topic. For a rigorous treatment of the thermodynamics of CNT see Ref. [82-84].

The process of freezing for a single particle is governed by the first order rate equation [79, 85, 86]:

$$\frac{-d\ln P(x,t)}{dt} = J_V(T)\cdot V\ (x) + J_S(T)\cdot S\ (x) \qquad 3.15$$

$P(x,t)$ is the probability that the particle is still unfrozen at time t ($P(x,0)=1$). $x=\ln\left(\frac{r}{u}\right)$ is the logarithm of the particle radius r in units of $u=1\,\mathrm{nm}$. $J_V(T)$ and $J_S(T)$ are the volume nucleation rate and the surface nucleation rate, respectively. $V(x)=\frac{4}{3}\pi\ e^{3x}$ and $S(x)=4\pi\ e^{2x}$ are the particle volume and the particle surface area, respectively. T is the temperature. Equation 3.15 includes both volume and surface contribution to nucleation. If freezing is exclusively a volume process the surface term equals zero and vice versa. In contrast to a single particle the crystallization kinetics of a particle ensemble no longer follows a simple first order rate law. The full treatment yields:

$$\overline{P}(t) = \frac{\int f(x,t)\cdot V(x)\cdot e^{-\left(J_V(T)\cdot V(x)+J_S(T)\cdot S(x)\right)\cdot t}\,\mathrm{d}x}{\int f(x,t)\cdot V(x)\,\mathrm{d}x} \qquad 3.16$$

where $f(x,t)$ is the size distribution of the droplet ensemble and $\overline{P}(t)$ is the average volume fraction of droplets that are still unfrozen at time t ($\overline{P}(0)=1$). Note that the

volume-weighted size distribution $f(x,t)V(x)$ appears because $\overline{P}_{\exp}(t)$ is derived from measurements that are proportional to the volume.

Even though Equation 3.15 is only valid for a single droplet, it has been used in previous investigations to describe droplet ensembles by simply replacing the droplet's volume and surface area *ad hoc* with their respective mean values $\overline{V}$ and $\overline{S}$ [25]. The suitability and implications of such approximations are critically examined in chapter 4.3.4 in relation to whether or not surface nucleation is an important process in the freezing of aerosols.

CHAPTER 4

CHF_3 AEROSOL PARTICLES

4.1 Introduction

As discussed in chapter 1, investigating aerosol particles with infrared spectroscopy is of interest for several reasons. One is the fundamental question of how intrinsic properties of aerosol particles manifest themselves in vibrational spectra. Specifically what determines the spectral features of molecularly structured aerosol particles and how we can use that knowledge to either predict or understand systems of interest. Such knowledge is essential for investigating dynamic processes in particles, for example their crystallization kinetics. This is the subject of chapter 4.3 which tackles a long standing debate on the nature and importance of surface nucleation processes. This is made possible with the improvement of the kinetic treatment, whereby the effects of ensemble average are correctly taken into account. Experimental techniques where measurements are performed on unsupported free particles in thermal equilibrium and in the submicron size range are a prerequisite to be able to clarify this issue. As is shown in section 4.3 fluoroform (CHF_3) constitutes a particularly suitable model system for analyzing nucleation kinetics because of its clear and distinct spectral signature of phase transitions.

In addition to the fundamental interest in intrinsic properties and crystallization dynamics of small particles (section 1.1), the formation of aerosol particles is also important for technical processes. One example of this is the formation of drug

nanoparticles by the Rapid Expansion of Supercritical Solutions (RESS) [14, 87]. Whereby a drug of interest is dissolved in a supercritical solvent and then expanded through a small nozzle, resulting in supersaturation and thus particle formation. Typical solvents used for this application are CO_2 and CHF_3. Previous investigations have looked at the solvent CO_2 [72, 87], but much less is known about the solvent CHF_3. The RESS process is therefore another motivation to investigate CHF_3 aerosols. In the region close to the expansion, before the Mach disc, both the drug and the solvent can co-condense to form small particles. The condensation of the solvent thus influences the formation of the drug particles. It is therefore of interest to know whether the solvent forms liquid droplets, amorphous particles or crystalline particles. In order to identify these different phases and their behaviour, as well as other possible changes in the architecture or shape of the particles, systematic experimental studies, complimented by modeling are needed. This is the subject of sections 4.4 and 4.5.

4.2 Experiment

CHF_3 particles were generated in a collisional cooling cell (chapter 2.2) by rapid injection of CHF_3/He gas mixture into a He bath gas at liquid nitrogen temperature (78K). The bath gas pressures ranged from 200 to 1000 mbar and consisted of commercially available He (99.995%, Praxair) that was further dried before use by passing it through liquid nitrogen cooling traps in order to minimize trace water impurities for measurements on pure CHF_3 particles. Sample gas mixtures contained 300-50000 ppm CHF_3 (99.995%, Spectragases) in He. Supersaturation of the sample gas following injection caused nucleation and condensation into particles. Their size, shape

and phase can be influenced by experimental conditions such as the concentration of the sample gas, as well as the pressure and temperature of the bath gas [14]. The progressive crystallization of the droplet ensembles (m.p. of bulk CHF_3 is 118 K) was then monitored *in situ* by rapid-scan FTIR spectroscopy.

As explained in sections 4.4.3, the crystallization of the supercooled liquid droplets and the shape change of solid particles happen simultaneously for *pure* fluoroform particles. To separate the time scales of the two processes, traces of water (0.1% to 6% of the fluoroform content) were mixed into the gaseous fluoroform samples in order to speed up the crystallization process. When these gas mixtures were introduced into the cold cell, water condensed first to tiny solid ice particles which served as condensation nuclei for the formation of supercooled liquid CHF_3 droplets. Once the liquid droplets were formed, the tiny solid water cores acted as nuclei for the heterogeneous crystallization of fluoroform droplets, which proceeds much faster than the crystallization via homogeneous nucleation, prevalent in pure fluoroform particles. This allowed the crystallization process to be separated in time from the subsequent slower shape changes of the crystalline particles discussed in sections 4.4.3 and 4.5.3.

4.3 Crystallization Kinetics

The mechanism behind homogeneous nucleation and crystallization in sub-micron aerosol droplets is the topic of numerous investigations and is still hotly debated [20-24, 86, 88-92]. The interest in phase transitions in finite-size systems encompasses aspects of both applied and fundamental sciences. To name but one example, the crystallization kinetics of supercooled sub-micron water droplets and nitric acid dihydrate aerosols turns out to be important for the formation of clouds in Earth's atmosphere, thus influencing the climate by various physical and chemical processes. The determination of corresponding crystallization rates has been the subject of numerous laboratory investigations [91-98]. By re-analyzing some of these data, Tabazadeh and coworkers [20, 22, 23] have sparked a controversy regarding particle crystallization by homogeneous nucleation. The main question is whether the kinetics are determined by volume nucleation or by surface nucleation, i.e. if the freezing rate is proportional to the volume or to the surface area of the particle. Although experimental evidence for surface crystallization in thin films has been reported [99], so far no experimental study has been able to prove unambiguously the importance of surface nucleation in small molecularly structured aerosol particles. The reason lies in the major experimental difficulties to observe crystallization processes in *unsupported* and *sub-micron-sized* aerosol particles under well defined experimental conditions. Particles collected on a substrate cannot provide reliable information because the interaction of the substrate with the particles surface can strongly influence surface nucleation processes. The observation of crystallization processes in single free-falling or single levitated aerosol particles is currently restricted to much larger, micron-sized particles [86, 91, 98], where

homogeneous freezing rates are found to be proportional to the volume. Hence for these particles, surface nucleation is negligible, and not surprisingly so given their high volume to surface ratio.

For single aerosol particles in the nm-size range, small enough that surface nucleation might become important, levitation and sensitive detection of crystallization processes is currently impossible. Investigations in this size range must then rely on particle ensembles, generated either in supersonic expansions [95, 100] or in aerosol chambers [90, 93, 94, 96], to determine freezing rates by electron diffraction or infrared spectroscopy. Most of these studies have interpreted the experimental data in terms of volume freezing, but after re-analyzing some of these data, Tabazadeh and coworkers have challenged this interpretation. They conclude that nucleation takes place preferentially at the surface rather than throughout the volume [20, 22, 23]. This has revived the current dispute regarding the issue. In all these studies with particle ensembles the apparent dominance of volume or surface nucleation was deduced from fitting experimental nucleation rates. These derivations used various approximations to account for the distribution of particle sizes in the freezing process, but very little if any attention has been paid to the influence of those approximations on the results. The discussion of experimental uncertainties and their effects has remained likewise incomplete. The following sections are an attempt to remedy the situation by critically examining the influence of approximations previously made and the limitations of currently available experimental techniques, on a suitable model system, fluoroform [25].

4.3.1 Spectral Deconvolution

To estimate the extent of crystallization at any given time during the crystallization process, a deconvolution of the experimental spectra was performed. The CH-bending vibration (ν_4 band) of fluoroform (figures 4.1 and 4.6) undergoes a continuous transformation from a broad, slightly asymmetrical band shape corresponding to a supercooled liquid state to a band shape with four sharp peaks characteristic for crystal field splitting. A deconvolution of the intermediate spectra is performed by adding together the spectra of completely liquid and completely crystalline particles with different weights and visually comparing it to the intermediate spectra. From these linear combinations the average volume fraction of unfrozen particles, or equivalently the probability $\overline{P}_{\exp}(t)$ that a particle remains unfrozen at time t can be determined for each intermediate spectrum from the integrated band strengths of the liquid component ($I_u(t)$) and the crystalline component ($I_f(t)$) of the spectrum:

$$\overline{P}_{\exp}(t) = \frac{V_u(t)}{V_u(t)+V_f(t)} = \frac{I_u(t)}{I_u(t)+I_f(t)}. \qquad 4.1$$

$V_u(t)$ and $V_f(t)$ are the total volumes of liquid particles at time t and crystalline particles at time t, respectively. $I_u(t)$ and $I_f(t)$ are determined by integration over the liquid and the solid component of the spectrum from 1400 to 1350 cm^{-1}. The integrated band strengths are proportional to the volume of the particles. A fully crystalline spectra is identified as one where spectral features remain constant over time. Deconvolution of spectra close to the end of crystallization leads to less accurate estimates of the probability to remain unfrozen. This is because of the broad nature of the liquid phase

and the predominant crystalline peaks. The contribution of the liquid phase towards the end of crystallization is difficult to estimate due to the loss of signal from the diffusion of particles out of the beam path. This accounts for most of the experimental uncertainty and can not be easily overcome.

Figure 4.1 gives an example for the deconvolution of experimental spectra. Trace b shows an intermediate spectrum in the region of the ν_4 vibration of CHF_3 (full line) together with its reconstruction (red line) as a linear combination of liquid and crystalline spectra. The match is almost perfect. The ability to observe the progressive crystallization of the particle ensembles up to completion together with the high time resolution of the rapid-scan FTIR measurements (ms) provides a uniquely complete experimental data set for the investigation of particle freezing mechanisms.

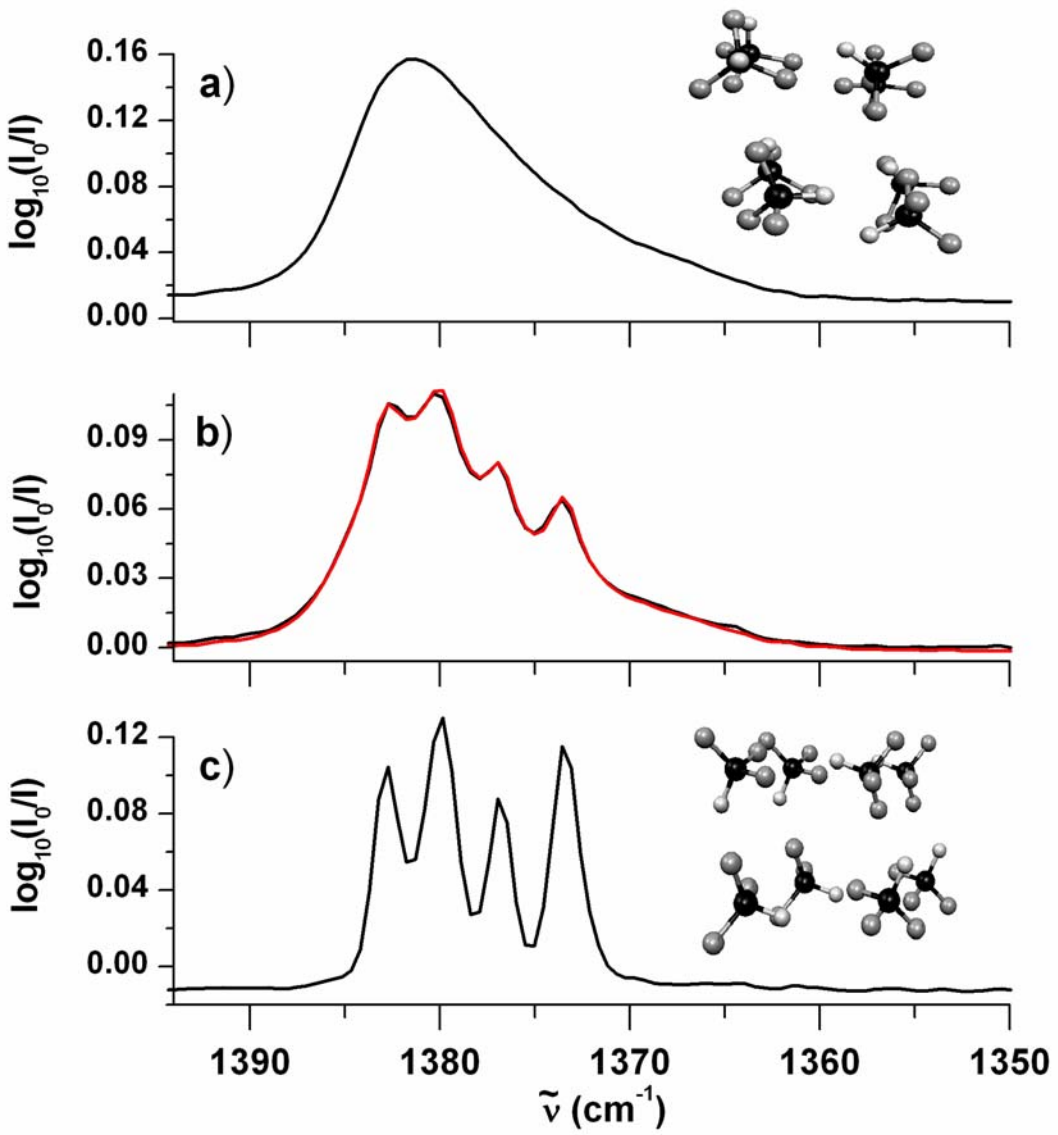

Figure 4.1. Experimental infrared spectra of freezing fluoroform aerosol particles in the ν_4 band region. (a) Initially formed supercooled liquid droplets. The molecules in these droplets do not show any long-range order [101]. (b) Intermediate spectrum. 18% of the whole droplet ensemble is frozen at this time. The red line represents a linear combination of spectrum a and c. (c) Crystalline aerosol particles after crystallization is complete. The band structure arises from the long-range order of the molecules in this phase [102].

4.3.2 Particle Size Determination

To calculate the average volume fraction of particles $\overline{P}(t)$ that are still unfrozen at time t in Eq. 3.16, the size distribution $f(x,t)$ has to be known (see section 3.2). In our cooling cell the size distribution changes with increasing time after aerosol formation. IR spectra that show a rise in baseline due to scattering can be used to estimate particle sizes with the help of Mie theory calculations (chapter 3.1.1). In order to perform Mie fits, refractive index data in the mid-infrared region is required. Literature values for fluoroform are not available so the refractive index data for NH_3 was used. Here it is assumed that the two substances scatter light with similar effects where they do not absorb strongly. We correct for the difference in absorption by comparing (normalizing) the square of the transition dipoles for the ν_2 mode in ammonia to the ν_2/ν_5 mode in fluoroform. The integrated absorption band for the ν_2 mode in ammonia is a factor of 4.99 smaller than that of fluoroform. It is assumed that the particle ensemble is best described by a standard log-normal distribution (see discussion on pages 90-93 in reference [103]) given by:

$$f(x,t) = N \frac{1}{\sqrt{2\pi}} \frac{1}{\ln(\sigma)} e^{-\frac{(x-x_0(t))^2}{2(\ln(\sigma)^2)}} \qquad 4.2$$

Where σ is the geometric standard deviation. N is the particle number density. $x_0(t) = \ln\left(\frac{r_0}{u}\right)$, where r_0 is the mean particle radius at time t and $u = 1\text{nm}$. It is not possible to refine all parameters σ, N, and r_0 at the same time. σ and r_0 turn out to be correlated [58]. Therefore σ is set to a fixed value and r_0 is refined. Another parameter needed for the calculations is the refractive index of the surrounding medium (set to 1.0).

A typical value for σ in cooling cells is 1.6. The effect of changing this value in the range between 1.2 and 2.0 is discussed in section 4.3.5 below. These two values represent the lower and the upper limit for possible values of σ in collisional cooling cells. During the experiments the mean radius r_0 increases and the number concentration N decreases with increasing time. For this reason a new size distribution has to be fitted to every measurement taken at later times during the experiment. The increase of the mean radius comes most likely from evaporation of small particles and re-condensation on larger particles. Agglomeration of particles is also possible. The decrease in the number concentration is due to diffusion losses of particles to the cell walls, and possibly also from evaporation of small particles. The refinement generally produces less ambiguous results for experimental spectra with higher to moderate scattering and higher absorption. Typically the mean particle radius increased during a measurement from roughly a 100 nm at the start of crystallization up to approximately 700 nm at the end.

4.3.3 Determination of Particle Crystallization Rates

Once spectral deconvolution and size distribution estimates have been performed for a specific experiment, the crystallization rates (J_V and J_S) can be determined. Eq. 3.16 gives the relation for homogeneous crystallization over time t as a function of both volume and surface nucleation rates (J_V, J_S). The rates are temperature dependent. Under the experimental conditions temperature is kept constant while the particle size changes over time as can be seen by an increase in scattering discussed in the previous section.

A program has been written that performs a non-linear least squares fitting of the data, taking the size change into account. Here a simple approximation of mean size and first order kinetics is no longer valid to treat the data and can give rise to false results. This is critically addressed in the following section. The input parameters for the fitting procedure are the experimental data points with the measurement time elapsed, logarithm of the probability to remain unfrozen and its uncertainty. Also a polynomial fit to the change in size as a function of time is needed and an estimate of the geometric standard deviation of the size distribution (normally taken to be 1.6) as is for the size determination. Fitting then proceeds by an initial guess and optimizes either one or both J_V and J_S simultaneously. Goodness of fits is calculated as the deviation from the fit line given by the χ^2 value, in addition to visually comparing it to the experimental data points. An example of fits where J_V and J_S are refined separately and simultaneously is shown in Figure 4.3. A list of obtained nucleation rates for various individual experiments and conditions is provided in Table 4.1.

Table 4.1 Homogeneous nucleation rates (in bold) of fluoroform aerosol particles for different concentrations and pressures. Pure volume nucleation rate J_V (for $J_S = 0$) and pure surface nucleation rate J_S (for $J_V = 0$) have been refined separately as well as together (last two columns). χ^2 is the calculated value for the goodness of fit. All measurements were performed at 78 K.

Gaseous Conc.	P [mbar] Cell/Line	Crystallization t_{start} [s]	t_{end} [s]	$r_{0,start}$ [nm]	$r_{0,end}$ [nm]	J_V [$cm^{-3}s^{-1}$]	χ^2	J_S [$cm^{-2}s^{-1}$]	χ^2	$J_V + J_S$ [$cm^{-3}s^{-1}$+$cm^{-2}s^{-1}$]	χ^2
0.07%	800/1500	290	770	100±20	400±50	**$1.7*10^{9}$**	$3.1*10^{-3}$	**$2.9*10^{4}$**	$2.6*10^{-3}$	**$4.2*10^{8}$ + $2.1*10^{4}$**	$2.4*10^{-3}$
1%	400/1000	290	815	120±20	450±70	**$1.2*10^{9}$**	$6.5*10^{-5}$	**$2.0*10^{4}$**	$8.8*10^{-4}$	**$1.0*10^{9}$ + $2.1*10^{4}$**	$7.5*10^{-5}$
1%	500/650	220	1060	100±20	500±70	**$6.1*10^{8}$**	$3.8*10^{-4}$	**$1.3*10^{4}$**	$2.9*10^{-4}$	**$1.9*10^{8}$ + $8.2*10^{3}$**	$2.0*10^{-4}$
3%	200/300	130	580	110±20	600±80	**$1.2*10^{9}$**	$3.0*10^{-4}$	**$2.4*10^{4}$**	$1.1*10^{-3}$	**$1.2*10^{9}$ + $4.3*10^{-2}$**	$3.1*10^{-4}$
3%	300/400	150	760	105±20	320±50	**$2.1*10^{9}$**	$3.0*10^{-3}$	**$3.0*10^{4}$**	$4.8*10^{-3}$	**$2.1*10^{9}$ + $4.9*10^{1}$**	$3.1*10^{-3}$
3%	400/500	240	980	150±20	650±80	**$2.4*10^{8}$**	$1.0*10^{-3}$	**$7.2*10^{3}$**	$1.3*10^{-4}$	**$4.9*10^{2}$ + $7.1*10^{3}$**	$8.8*10^{-5}$
3%	500/600	470	1050	170±30	530±70	**$2.3*10^{8}$**	$1.3*10^{-4}$	**$5.3*10^{3}$**	$1.4*10^{-4}$	**$2.2*10^{8}$ + $5.1*10^{2}$**	$6.2*10^{-4}$
5%	200/300	100	440	120±20	500±70	**$2.3*10^{9}$**	$9.8*10^{-5}$	**$4.0*10^{4}$**	$5.1*10^{-4}$	**$2.0*10^{9}$ + $5.5*10^{3}$**	$9.2*10^{-5}$
5%	500/600	230	900	130±20	700±100	**$2.3*10^{8}$**	$2.2*10^{-4}$	**$6.9*10^{3}$**	$7.6*10^{-5}$	**$1.0*10^{8}$ + $4.4*10^{3}$**	$1.6*10^{-4}$

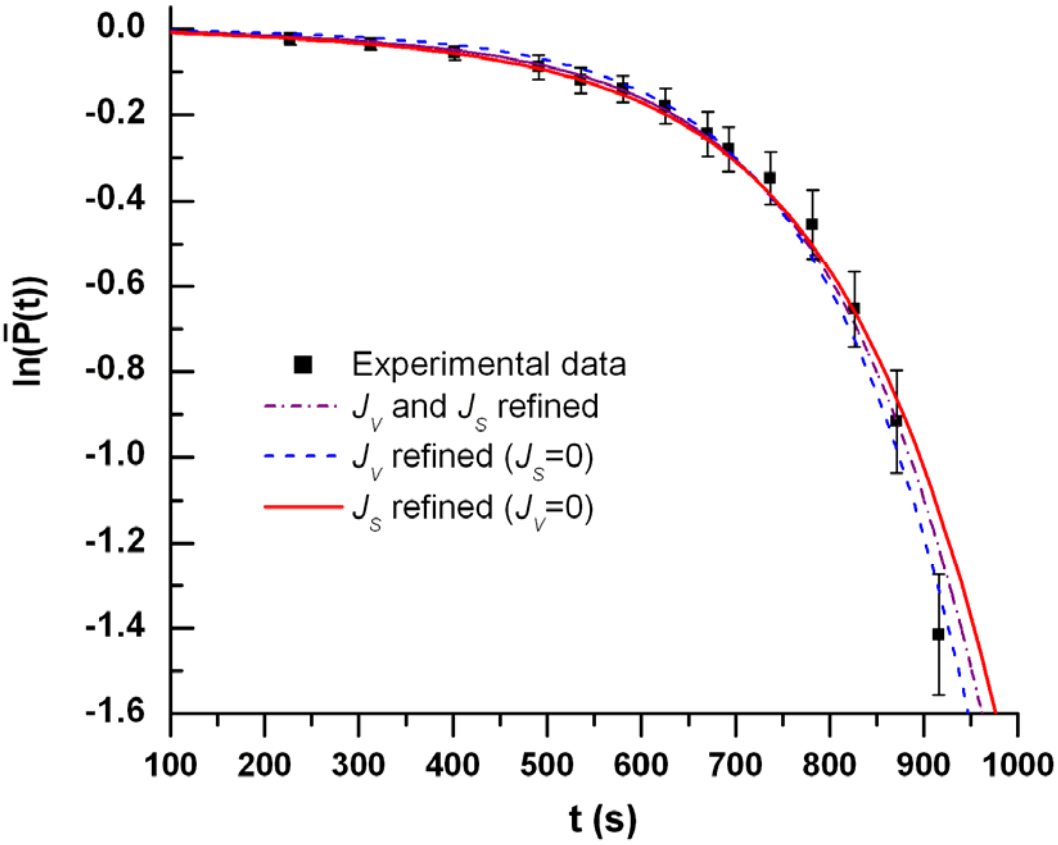

Figure 4.2 The logarithm of the fraction of unfrozen aerosol droplets ($\ln \overline{P}(t)$) is depicted as a function of time *t*. Squares: Experimental data points. Purple dash dot line: Fit under the assumption that both volume and surface nucleation contribute. Blue dash line: Fit for pure volume nucleation (constraint $J_S = 0$). Red Thick line: Fit for pure surface nucleation (constraint $J_V = 0$).

4.3.4 Effect of Approximate Equations for *P(t)*

Equation 3.15 includes both the possible volume and surface contribution to nucleation. So that if droplet freezing is exclusively a volume process the surface term equals zero and vice versa. Even though Equation 3.15 is only valid for a single droplet, it has been used (in stead of Equation 3.16) in previous investigations to describe droplet ensembles simply by replacing the droplet's volume and surface area ad hoc with their respective mean values $\overline{V}$ and $\overline{S}$. Then Equation 3.15 becomes:

$$\frac{-d\ln\overline{P}(t)}{dt} = J_V(T)\cdot\overline{V} + J_S(T)\cdot\overline{S} \qquad 4.3$$

The solution to Equation 4.3 is:

$$\overline{P}(x,t) = e^{-\left(J_V(T)\cdot\overline{V}+J_S(T)\cdot\overline{S}\right)\cdot t} \qquad 4.4$$

Where $\overline{P}(t)$ is the average volume fraction of droplets that are still unfrozen at time t ($\overline{P}(0)=1$). With $\overline{V}$ and $\overline{S}$ estimated or determined from the droplet size distribution using various approximations [22, 23, 90, 93-96, 100]. The volume nucleation rate J_V and the surface nucleation rate J_S have been determined by non-linear least squares fits of $\overline{P}(t)$ to the experimentally determined average volume fraction of unfrozen droplets $\overline{P}_{\exp}(t)$. Such fits have provided the basis to decide whether or not surface nucleation is important.

The following demonstrates that Equation 4.4 represents a very crude approximation to the correct treatment of the crystallization kinetics of a droplet ensemble given by Equation 3.16. In particular, it is shown that trying to distinguish

between volume and surface nucleation becomes impossible, and that the approximation strongly affects experimental nucleation rate constants.

Figure 4.3 compares the full treatment of Equation 3.16 with the approximation given in Equation 4.4 for a model case. An artificial data set (triangles) calculated with the correct expression in Equation 3.16 with $J_V = 1.2 \cdot 10^9\ \mathrm{cm^{-3}s^{-1}}$ (typical value found for CHF_3 droplets, see section 4.3.3) and $J_S = 0$ (no surface nucleation). A lognormal size distribution $f(x,t)$ was used, with a typical time dependence found experimentally for CHF_3 droplets (see previous section). The squares in Figure 4.3 thus mimic an experimental data set for pure volume nucleation. To calculate $\overline{V}$ and $\overline{S}$ (Equation 4.4) two classes of approximations are typically used in the literature: i) A mono-disperse aerosol with radius $\bar{r}$, $\overline{V} = \frac{4}{3}\pi\,\bar{r}^3$, and $\overline{S} = 4\pi\,\bar{r}^2$. We calculate $\bar{r}$ as the volume-weighted mean radius $\bar{r} = \frac{\int f(x,t)\, r(x)\, V(x)\, \mathrm{d}x}{\int f(x,t) V(x)\, \mathrm{d}x}$ (in some cases even cruder approximations have been used). ii) An aerosol with a volume-weighted mean volume $\overline{V} = \frac{\int f(x,t) V(x)^2\, \mathrm{d}x}{\int f(x,t) V(x)\, \mathrm{d}x}$ and a volume-weighted mean surface $\overline{S} = \frac{\int f(x,t)\, S(x)\, V(x)\, \mathrm{d}x}{\int f(x,t) V(x)\, \mathrm{d}x}$. The lines in Figure 4.3 represent fits to the artificial data set using the approximate Equation 4.4. Case ii) was used to calculate $\overline{V}$ and $\overline{S}$, but qualitatively similar results are also found for case i). The red dashed line represents a fit for which only J_V was refined and J_S was fixed to zero i.e. pure volume nucleation. The blue full line represents a fit for which only J_S was refined and J_V was fixed to zero i.e. pure surface nucleation.

Equation 4.4 is severely misleading when used to differentiate between volume and surface nucleation in the freezing of aerosols. The fit results in Figure 4.3 would lead to

the conclusion that the freezing of the model particle ensemble was dominated by surface nucleation even though the data points describe pure volume nucleation only. This evident contradiction makes it clear that the approximations implicit in Equation 4.4 are far too crude to allow the two processes to be distinguished. Hence we must conclude that the re-analysis of data in Ref. [22, 23] cannot provide any support for the dominance of surface nucleation claimed by the authors. Another important conclusion refers to the values of the rate constants previously determined by using Equation 4.4 or similar approximations [22, 23, 90, 93-96, 100]. Compared with the true values such approximations can lead to deviations of the rate constants of one order of magnitude. To account for this effect, published rate constants should be quoted with an uncertainty of a factor of ten.

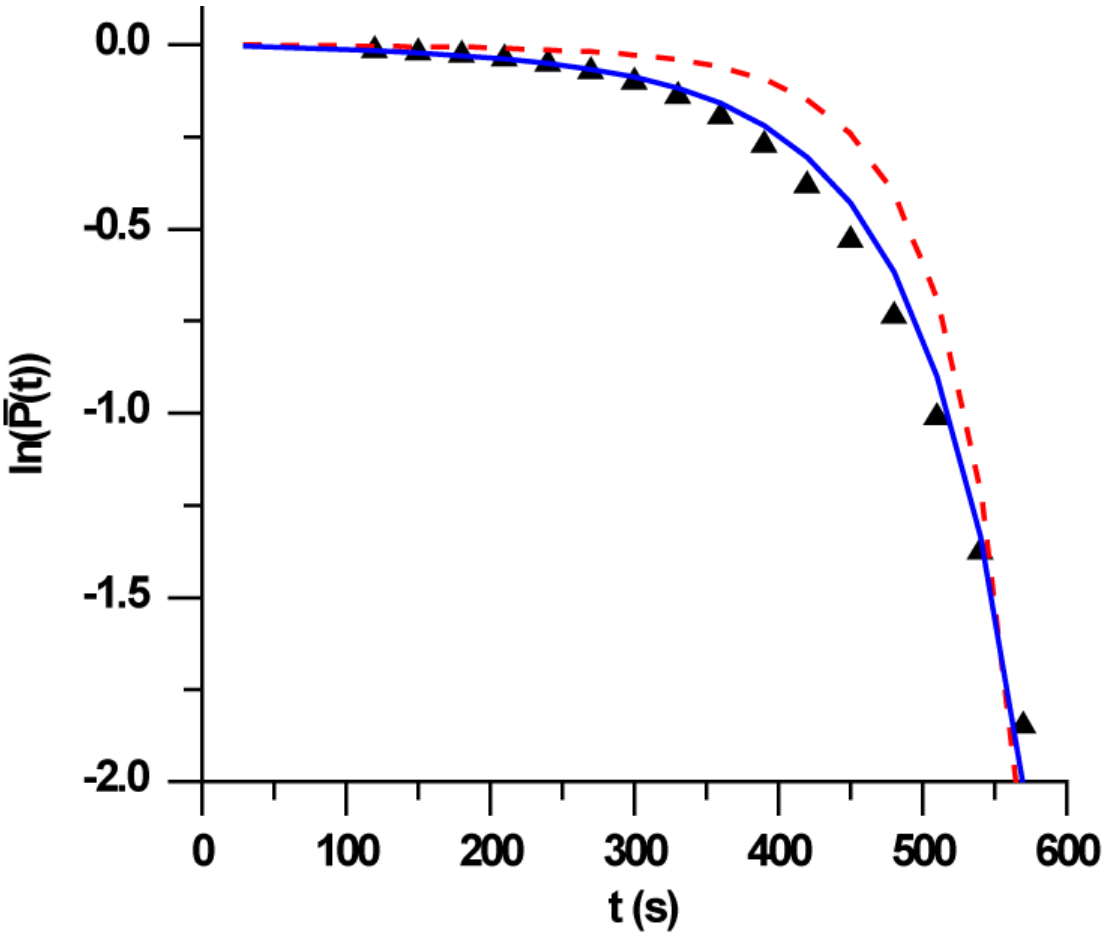

Figure 4.3. The logarithm of the fraction of unfrozen aerosol droplets ($\ln \overline{P}(t)$) as a function of time *t*. Triangles: Synthetic data set calculated from Equation 4 for pure volume nucleation (i.e. $J_S = 0$). Red dashed line: Fit to the squares using the approximations described in the text (Equation 4.4) under the assumption of pure volume nucleation ($J_S = 0$ constraint). Blue full line: Fit to the squares using the approximations described in the text under the assumption of pure surface nucleation ($J_V = 0$ constraint).

4.3.5 Conclusions on Surface vs. Volume Nucleation

When the results presented in Table 4.1 and Figure 4.2 are taken together it becomes clear that it is not possible to distinguish between the two mechanism based on the obtained nucleation rates. In Figure 4.3 it is illustrated for a particular experiment how typical experimental uncertainties associated with ensemble measurements in aerosol chambers can accommodate both possible nucleation mechanisms, with neither clearly favoured. As can be seen from Table 4.1, the same qualitative result (to within error bars) can be found for all experimental conditions and particle sizes that have been investigated. These results provide further evidence against claims of experimental support for surface nucleation [22, 23]. The highly non-linear error propagation greatly amplifies the uncertainties of experimental data. The experimental uncertainty that is taken into account arises from sources such as the choice of the geometric standard deviation σ (normally estimated to be around 1.6 for aerosol ensembles), the determination of integrated band strengths, the deconvolution of the intermediate spectra and ambiguity in assigning a mean particle size based on Mie calculations.

From these systematic studies it must be concluded that at present, the nucleation rates for particle ensembles cannot be determined more accurately than within approximately one order of magnitude. This is despite the fact that the proper ensemble average (Equation 3.16) has been accounted for. These results comprise the first clear proof that with currently available measurement techniques it is impossible to distinguish between volume and surface nucleation of freezing aerosol droplet ensembles in the sub-micron size range. This finding is consistent with the comments and conclusions made in Refs. [86, 88, 89, 92], but contradicts the claims put forward in Refs. [22, 23, 90, 94-96,

100]. The problem can be attributed to two distinct sources. They are the experimental uncertainties associated with those measurements and approximations commonly used to determine the kinetics. While the latter can be avoided with a proper ensemble average (Equation 3.16), the former are inherent to the experimental techniques currently available. Both sources contribute approximately a factor of ten each to the relative uncertainty of published experimental nucleation rates. In the absence of evidence for the dominance of volume nucleation or any influence of surface nucleation, both rate constants, J_V and J_S, should be specified to characterize the freezing kinetics of aerosol particle ensembles. These general results can have a wide range of implications and must be taken into account as uncertainties in the current modeling of aerosol nucleation processes in the atmosphere until the nucleation mechanism is clarified and more accurate rate constants become available. Ideally this should be done by measurements on single unsupported sub-micron sized particles. It is in the size region from a few nanometers up to a few microns where the difference in contributions from surface versus volume nucleation becomes important. This is simply the result of higher volume droplets having a much higher probability to nucleate from within, given the limited number of molecules at the surface compared to the bulk. Likewise, very small particles (less than a few nm) have most of their molecules located at the surface, and therefore nucleate from there.

As is seen in table 4.1, nucleation rates of submicron sized fluoroform aerosol droplets are generally found to be in the range of $J_V = 10^8\text{-}10^{10}$ cm^{-3} s^{-1}, $J_S = 10^3\text{-}10^5$ cm^{-2} s^{-1} at 78K. Those rates sensitively depend on the way heat is released and thus on the experimental conditions. Due to the large uncertainty of the obtained nucleation rates

from the inherent experimental limitations and the practical difficulty to separate the effects of each variable, the rate constant dependence on experimental conditions, such as pressure and concentration is difficult to determine. In table 4.1 there are however some trends that suggest that homogeneous nucleation rates are higher at lower cell pressure (200 mbar) than higher (500 mbar) cell pressure.

4.4 Spectral Signatures of Crystallization and Shape Change

Measuring infrared spectra of aerosols particles can potentially provide us with a wealth of information about the dynamic processes that they undergo. Fluoroform aerosol particles turn out to be a particularly well suited system to study two distinct dynamic processes, their crystallization behaviour and shape changes [49]. The structure of all the mid-infrared active bands characteristically depends on the internal structure of the particles. This can be seen in Figure 4.4 for the CF_3 stretching modes ν_5/ν_2 and Figure 4.5a for the CH bending vibration ν_4 and the CF_3 deformation mode ν_3. Under the conditions that were studied, the aerosol particles can exist in two distinct phases. Initially all are in a completely disordered state and subsequently the transition to the crystalline monoclinic phase takes place, which is also found in the bulk [102]. Identification of the crystalline phase was made by comparing the shape and band positions of the ν_4 mode of aerosol particle spectra to the published bulk spectra. The only band in the infrared spectra that is also sensitive to the particles' shape is the ν_5/ν_2 band system around 1140 cm^{-1} (Figure 4.4b). The band structures of the ν_3 vibration around 696 cm^{-1} and ν_4 vibration around 1378 cm^{-1} are not affected by the shape of the aerosol particles (Figure 4.5b).

In order to explain this fact we need to look at the difference in the strengths of molecular transition dipoles for each band. The ν_5 band has a strong transition dipole (see Table 4.2 and Ref. [104]) that gives rise to strong exciton coupling between all molecules in an aerosol particle. The ν_2 band lies very close to the ν_5 band and is therefore also involved in the coupling. As previously explained in section 3.1.2 and references [14, 16,

64] the degeneracy of the uncoupled molecular eigenstates is lifted and the vibrational eigenfunctions become delocalized over the whole aerosol particle, making them sensitive to the particle shape. By contrast the ν_3 and ν_4 vibrations have only small transition dipoles [104, 105] so that the exciton coupling and shape effects become negligible for the band structures of these two bands.

This distinct behaviour of mid-infrared bands makes it possible to distinguish between the crystallization process of aerosol particles and the shape changes of the crystalline particles once formed. These two processes are shown as a function of time in regions of the ν_5/ν_2 band in Figure 4.4, and in the ν_3 and ν_4 band region in Figure 4.5. The figures are separated into two panels; Panel a shows the evolution of the spectra during crystallization while panel b shows the evolution of the spectra during the subsequent shape change. All changes in the spectra occur continuously as time elapses after the particles have formed (t = 0 s). For the sake of clarity, only twenty snapshots of the recorded particle spectra are shown for selected times. In principle it is possible to observe the entire process with millisecond time resolution. Figures 4.5 and 4.6 are from an experiment where the two processes are clearly separated in time. Signs of shape changes only start to emerge (t = 71 s) after the crystallization process is complete (t = 38 s). As explained in section 4.2 and further discussed below, this separation of time scales was achieved by having traces of small water ice nuclei present to accelerate the crystallization. This does however not affect the general conclusions.

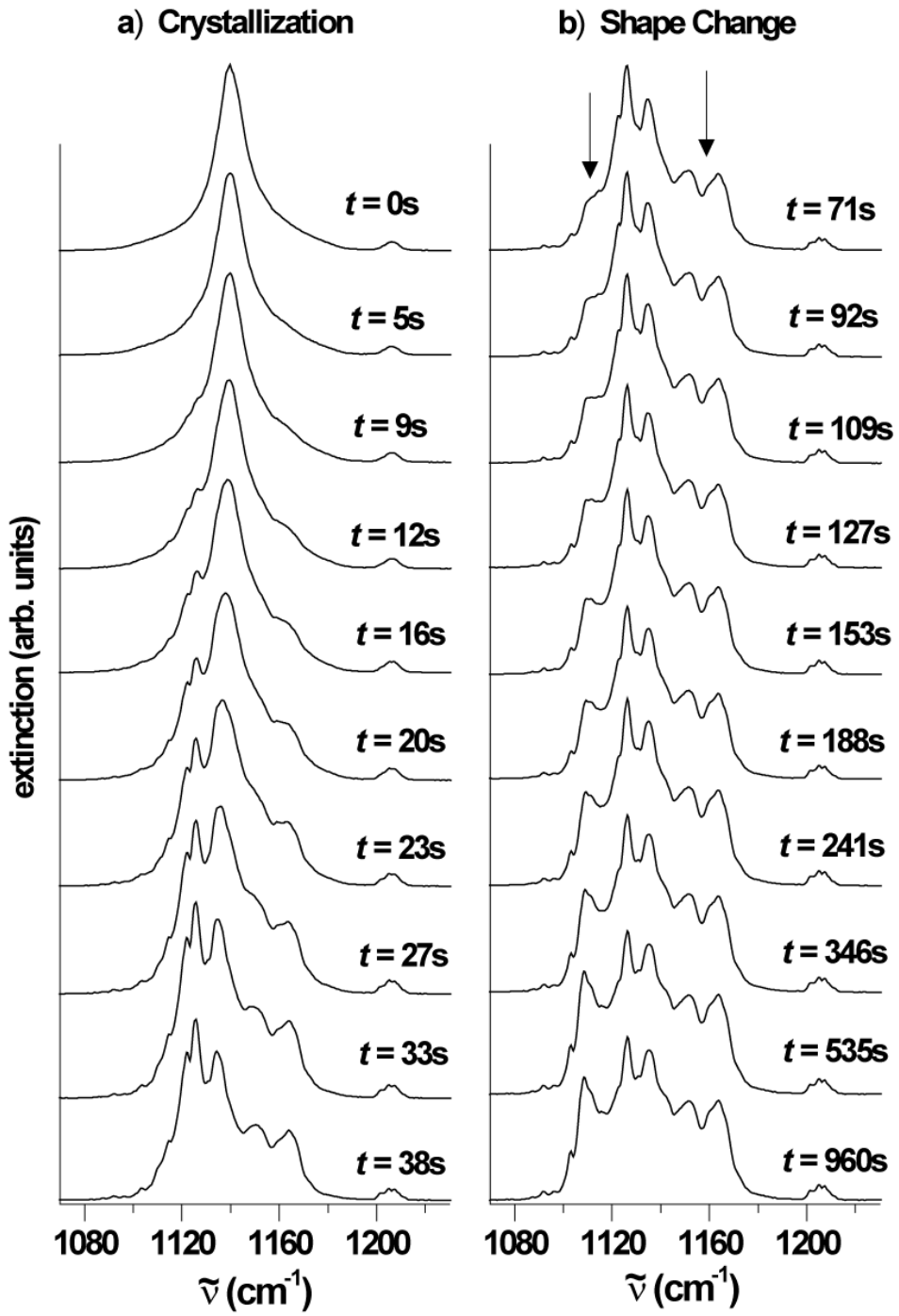

Figure 4.4 Time dependent infrared spectrum of CHF_3 aerosol in the region of the ν_5/ν_2 bands. a) Temporal evolution during the crystallization of the particles in the presence of trace amounts of water ice nuclei. b) Temporal evolution during the change of the particles' shape from cube like to elongated particles. *t* is the time after the particle formation (*t* = 0 s).

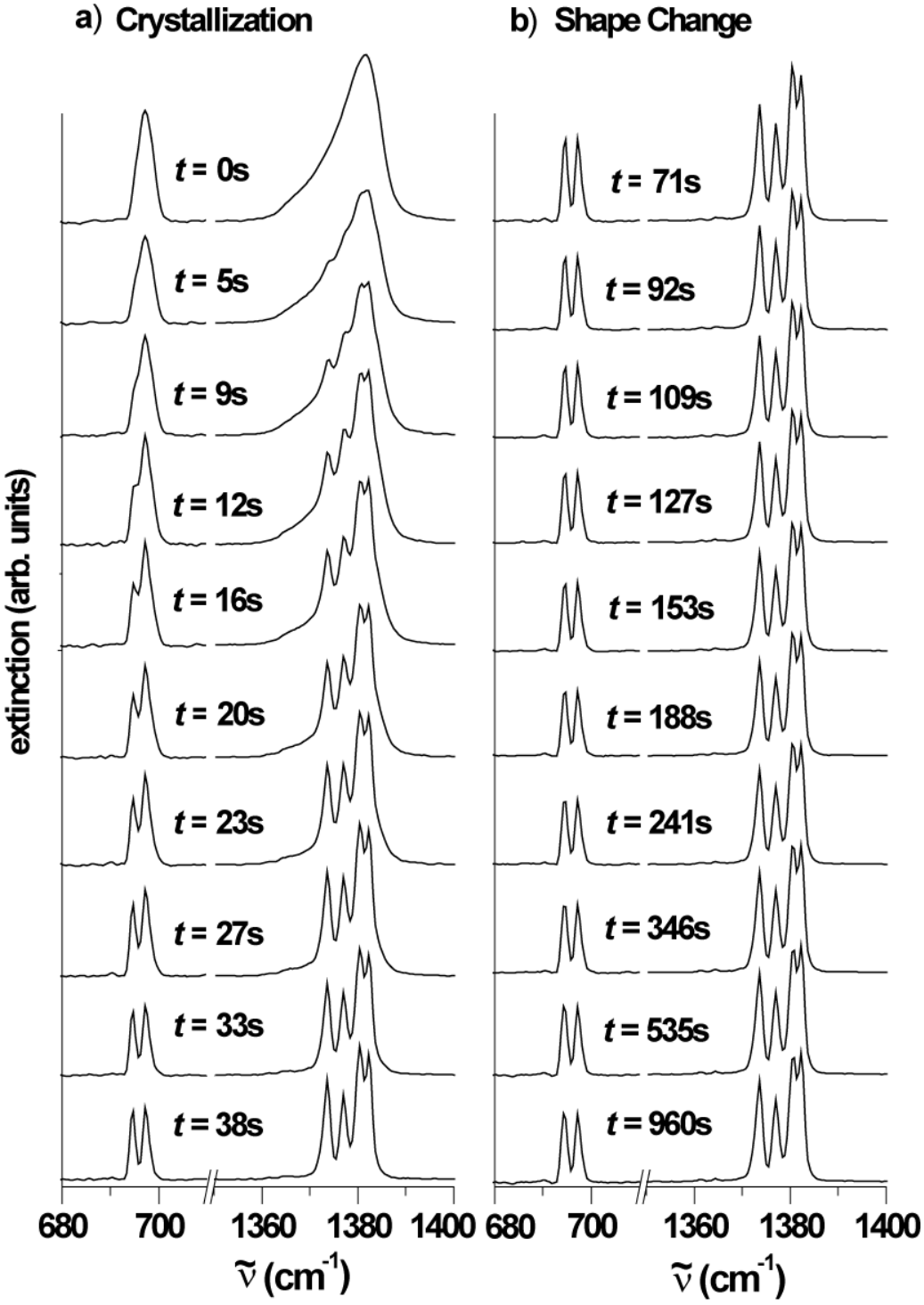

Figure 4.5 The same as in Figure 4.4 but in the regions of the ν_3 and ν_4 bands.

4.4.1 Supercooled Liquid Fluoroform Droplets

One of the initial questions that arise when analyzing the aerosol spectra is the nature of the initial phase that the particles are formed in. The particle condensation from the gas phase happens at a rate much greater [106] than the time resolution of the spectrometer allows us to observe. This is because of the high level of supersaturation of the substance directly after injection into the cell. The first spectrum is therefore recorded immediately after particle formation, set to time t = 0 s in Figures 4.4 and 4.5. These spectra exhibit broad unstructured bands reflecting a high degree of disorder within the particles. There are two possibilities that could explain the observed band shapes, spherical amorphous solid particles or supercooled liquid droplets. Several considerations clearly point to the formation of the latter. Firstly, fluoroform has a broad liquid range extending over 73 degrees from 191 K down to 118 K. The degree of supercooling at 78 K is high but within the range of what is commonly observed for other substances (40 K for water). Secondly, phase changes to a metastable phase are common phenomena and have been formulated in Ostwald's rule of stages (Ostwald's Stufenregel) [107, 108]. These state that a crystallizing system progresses from the supersaturated state to equilibrium in stages, each stage representing the smallest possible change in free energy. This implies that the supersaturated gas phase does not directly transform into the most stable state, but rather into the next most stable or metastable state, which in this case would be the supercooled liquid. Thirdly, measurements done at temperatures slightly higher than the melting point of fluoroform show the same band shapes as measurements done at 78 K. The fourth argument comes from the partial pressure of fluoroform in the cell during particle formation. It lies 1-3 orders of magnitude above the extrapolated

vapour pressure of liquid fluoroform at 78 K [109], which in turn lies higher than the vapour pressure over the solid. This would favour the formation of liquid instead of solid particles. The final argument comes from the calculated infrared spectrum of a simulated amorphous solid particle (not shown here). The calculated ν_5/ν_2 band for the amorphous solid particle shows some structure, inconsistent with the unstructured experimental spectra. If all these arguments are taken together they clearly favour the formation of liquid supercooled droplets over amorphous solid particles.

4.4.2 Crystallization of Fluoroform Droplets

First signs of crystallization become apparent when the shape of the bands starts to deviate from the broad and unstructured ones found initially, to a more structured band shape. In the case where nucleation was initiated heterogeneously (as shown in Figures 4.4 and 4.5), this band splitting starts to occur within seconds after the droplets are formed and has completed after 38 s. Homogeneous nucleation takes longer to initialize and complete as can be seen in Table 4.1. A detailed discussion of homogeneous nucleation kinetics is presented in section 4.3. Independent of the mechanism of nucleation, the ν_3 and ν_4 bands show a splitting up into two and four sharp sub-bands respectively, identical to the splitting pattern (from crystal field splitting) of the crystalline bulk [102]. We can therefore conclude that fluoroform aerosol particles crystallize to a stable monoclinic space group $P2_1/C$ with four molecules per unit cell, same as in the bulk.

The ν_5/ν_2 band system displays behaviour that differs from what has just been described for the ν_3 and ν_4 bands. Its band structure is determined by strong transition

dipole coupling between the molecules that make up the particle. Hence this band system is not only sensitive to details in the internal structure of the particles, but also to the shape of the particles. By analyzing this band it becomes possible to determine the particle shape right after crystallization is complete (see sections 4.4.3 and 4.5).

The presence of water ice nuclei leads to much faster heterogeneous crystallization rates as can be seen by comparing the times in Figures 4.4 and 4.5 to values found in table 4.1, which are for homogeneous crystallization. The exact values of the rates depend on the size and number of the water ice nuclei present. Since these water ice particles are small enough that they do not scatter any light in the mid-infrared, their size is not accurately known beyond the upper limit of approximately 10 nm. Without this knowledge, accurate rate constants for the heterogeneous nucleation process can not be obtained.

4.4.3 Spectral Signatures of Shape Changes

After crystallization is complete at around t = 38 s and up until t = 65 s the band shapes in the mid-infrared remain unchanged. At this point the ν_5/ν_2 band system starts to undergo a second systematic change, shown in panel b in Figure 4.4. The ν_3 and ν_4 bands (Figure 4.5 panel b), however, do not undergo any further changes and remain constant for the duration of the measurement. For the ν_5/ν_2 band, a side band at around 1105 cm^{-1} grows with increasing time as well as relative increase in the overall 1145-1170 cm^{-1} region (indicated by arrows in the figure), as compared to the two stronger bands at ~ 1126 and 1135 cm^{-1}. The fact that only the ν_5/ν_2 band is sensitive to this second change clearly indicates that this change must influence the exciton coupling scheme within the aerosol particles. There are in principle three possibilities for this to happen. Firstly, this could be the result of a change in the internal structure (phase change). Secondly, the particles might be changing in size, and thirdly, this is due to changes in the shape of the particles. The first two possibilities, however, can be ruled out. The stability of the ν_3 and ν_4 bands after crystallization clearly speaks against a second phase change. Those bands would undoubtedly be sensitive to such a change, which would then be detected. Likewise the size of the particles cannot be the reason. This is because the band structure is not sensitive to the particular size in the size range considered here (see explanations in Refs. [64, 66]). The only possibility left is therefore a change in the particles' shape. To confirm that this is actually the case and to characterize the nature of these shape changes it becomes necessary to model them in some way. In the following section, the vibrational exciton model (section 3.1.2) is used to predict what effects the particle shape change might have on the spectra. It is shown by comparison with the experimental

spectra in Figure 4.4 panel b that the particle ensemble transforms from one with mainly cube-like particles to an ensemble with an increasing ratio of elongated particles. The timescale at which this occurs depends on the experimental conditions. Shape changes start earlier and happen faster at low bath gas pressure (200 mbar) in the cell compared to high bath gas pressures (800 mbar). The same trend is also found for higher sample gas concentrations (50000 ppm) compared to low sample gas concentrations (600 ppm).

As previously noted, the particular example shown in Figures 4.4 and 4.5 shows a case for which the two processes were separated in time, with crystallization completed before any shape changes take place. To achieve this separation the experimental conditions were tuned so that the crystallization process was accelerated and the shape changes were delayed. By choosing a high bath gas pressure in the cooling cell (800 mbar) it was possible to delay the onset of shape change. The crystallization process was accelerated by introducing a minor amount (up to 5.8% of the total fluoroform content) of small water ice nuclei, onto which fluoroform could condense. The heterogeneous crystallization that becomes possible in the presence of the water ice nuclei is much faster than the predominant homogeneous nucleation in the case of pure fluoroform droplets. Since the ice nucleus is tiny compared with the fluoroform particle as a whole they do not alter any of the spectroscopic features as seen for pure fluoroform particles. In both cases, the features of crystallization and shape changes look exactly the same. The only difference is that for pure CHF_3 particles the crystallization and shape change overlap in time because crystallization happens much more slowly. This is illustrated in Figure 4.6, with traces a and b showing the ν_4 band and ν_5/ν_2 band, respectively, recorded 1165 s after particle formation. The ν_4 band is not yet completely resolved into two sharp peaks,

a sign that some of the particles are still unfrozen at that time. At the same time, side bands in the ν_5/ν_2 system are emerging (see arrows), indicating that some crystalline particles have already adopted an elongated shape. As seen from the experiments, the final result is the same regardless of whether crystallization occurs concurrently or prior to the shape changes. Note however, that even though the two processes overlap they can still be distinguished from one another by deconvoluting the infrared spectra into its component parts as is described in section 4.3.1. The reason is that the crystallization time of a single droplet of the ensemble happens instantaneously compared to the shape change.

It is in principle possible to derive the kinetics of the crystallization process as well as the kinetics of the shape change of crystalline particles from time-dependent infrared spectra. The kinetics of the crystallization process of pure CHF_3 particles have already been reported in section 4.3. The emphasis there was to clarify the issue of surface versus volume nucleation (see also ref. [25]) and to see if the two processes could be distinguished based on their kinetics. No rate constants were derived for the change in the shape of the crystalline particles observed in Fig. 4.5. As discussed in the next section, only speculations are possible about the processes responsible for these shape changes. Without better knowledge of the processes involved and their mechanisms it is impossible to derive meaningful rate constants for the shape change. Any possible shape changes associated with the initial transition from liquid droplets to solid particles is addressed in section 4.5.1 with the help of the exciton model.

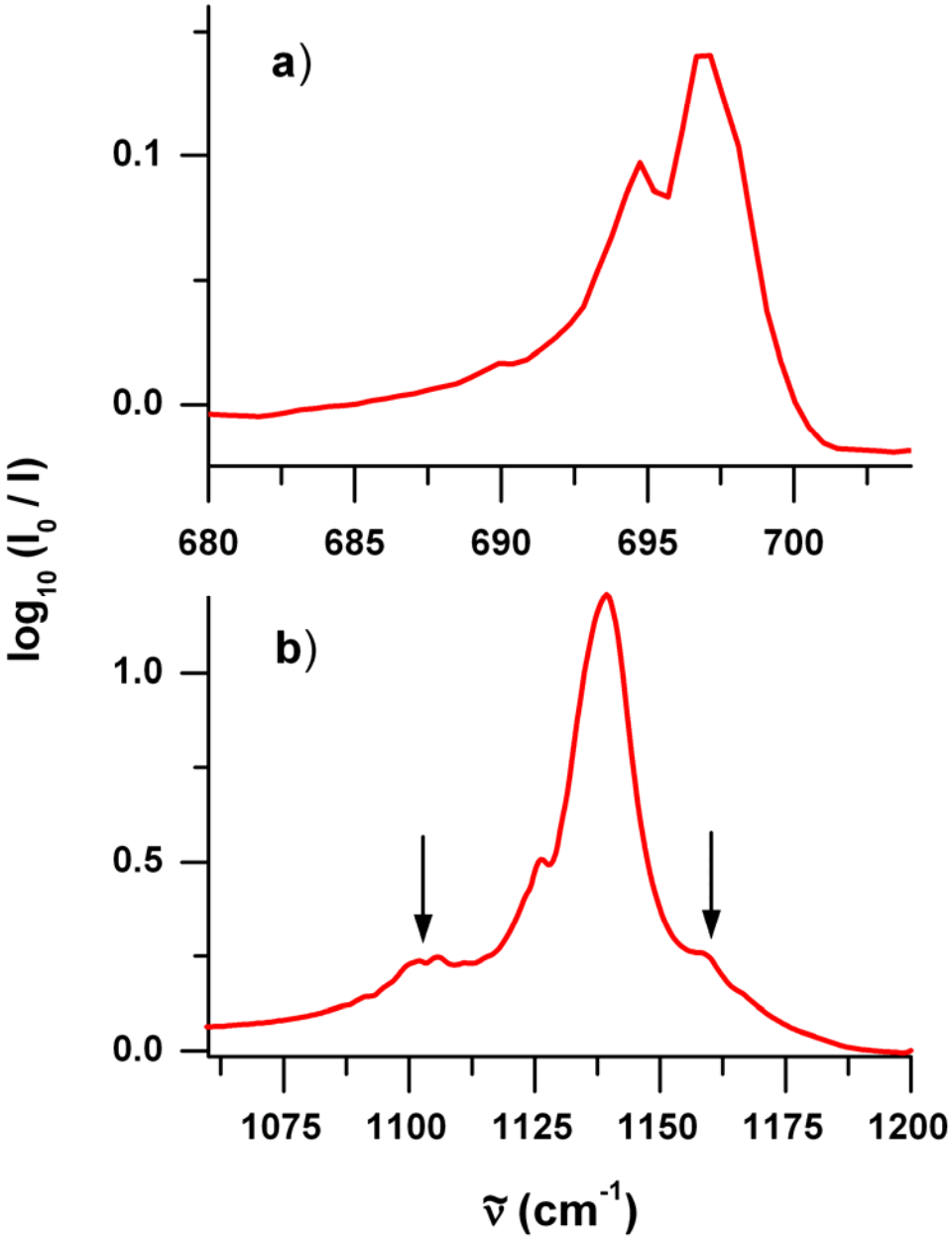

Figure 4.6 Experimental infrared spectrum of pure fluoroform particles recorded 1165 s after particle formation. a) Region of the ν_4 band. b) Region of the ν_5/ν_2 band, showing signs of elongated particle shape (arrows). Tails towards lower wavenumbers are due to elastic scattering of the light by the particles, which in this case had sizes in the upper nanometer range.

4.5 Analysis of Particle Shape by Exciton Calculations

As previously stated, the ν_5/ν_2 band system at around 1140 cm^{-1} is dominated by exciton coupling, making it sensitive to the shape of the aerosol particles. The comparison of model calculations of this band system for different particle shapes with the experimental infrared spectra thus allows us to find out more about the evolution of the particle shape as a function of time (Figure 4.4). The theoretical background of the model used in this study, the vibrational exciton model, is given in section 3.2. The corresponding input parameters used for the calculations in the region of the stretching vibrations ν_5/ν_2 are listed in Table 4.2 [104, 110]. The transition wavenumbers and the transition dipoles in Table 4.2 correspond to the mean values in different cryosolutions measured in Ref. [104]. Solution values were used rather than gas phase values [105] because they provide a better representation of the influence of a dielectric surrounding on a molecule. Calculations with gas phase values (not shown here) lead to similar results with only slightly broader bands shifted to higher wavenumbers.

Table 4.2 Spectroscopic parameters used in the vibrational exciton calculations of CHF_3 particles in region of the ν_5/ν_2 CF stretching vibrations. $\tilde{\nu}$ is the transition wavenumber, μ is the transition dipole, α is the polarizability, ε_0 is the vacuum permittivity.

Vibrational Mode	$\tilde{\nu}$ / cm^{-1}	μ / D	$\frac{\alpha}{4\pi\varepsilon_0}$ /Å^3
			2.89, 2.61 [2]
ν_5	1143.6 [1]	0.29 [1]	
ν_2	1136.3 [1]	0.18 [1]	

[1] Ref. [104]. $\tilde{\nu}$ corresponds to the mean values measured in the different liquids.

[2] $\alpha_{xx}= \alpha_{yy,} \alpha_{zz,}$ Ref. [110].

In Figures 4.4 and 4.5 we have two distinct types of shape changes occurring. The first one is associated with the crystallization of the supercooled liquid droplets (see traces a), and is the topic of the following section. The spectral changes associated with the second shape change (traces b) have already been described in the previous section. This second shape change takes place after crystallization is complete and thus corresponds to a shape change of the crystalline fluoroform particles. The nature of which is further clarified in section 4.5.2.

4.5.1 Identification of Cube-like Particles by Exciton Calculations

At time t = 0 s, liquid supercooled droplets are formed with a spherical shape. Crystallization of these droplets is likely to alter this shape in some way. Since individual particles of the ensemble crystallize almost instantaneously (compared to shape changes) they will presumably retain a shape with similar axis ratios directly after crystallization (t = 38 s, Figure 4.4), i.e. globular or cube-like. Figure 4.7 compares two exciton calculations (see section 3.1.2) for a crystalline spherical particle (trace a) and a crystalline particle with a cube-like shape (trace b), to an experimental spectrum measured directly after crystallization is complete (trace c, identical to the bottom trace of panel a in Figure 4.4). The simulation in trace b is for a monoclinic parallelepiped with equal side lengths obtained by extending the unit cell in the direction of the generating vectors. This form (rhombic prism) is a likely morphology based on the crystalline space group (see table 10.2.3 in [111]) and represents what can be called a cube-like particle. Note that other cube-like shapes, such as perfect cubes or quasi-octahedra (cubes with their corners cut off), have almost identical spectral features (results not shown here) and are therefore not treated separately.

The experimental spectrum consists of a broad band (roughly 70 cm^{-1}) with a maximum in extinction around 1130 cm^{-1} and pronounced secondary maxima at higher wavenumbers. The calculated exciton band structure for a spherical particle (trace a) does not reproduce these features. This is a clear sign that after crystallization is complete, the particles are no longer perfectly spherical. The main features of the experimental band structure are, however, well reproduced by exciton calculations of cube-like particles

(trace b). It is therefore possible to conclude that during the crystallization process the shape changes from spherical droplets to cube-like crystalline particles.

A perfect agreement between the calculations and experiment, especially for the complex ν_5/ν_2 band system, is not to be expected. First and foremost, these calculations represent true predictions based on first principles and a simplified model, no fits to the experimental spectra are performed. A better agreement with experiment might be possible by employing a more elaborate model such as the Extended Exciton Model [15], which treats intra- and intermolecular interactions in terms of appropriate force-fields to account for structural changes and local molecular variations of transition frequencies and dipole moments. Development of a sufficiently accurate force field for this purpose requires a significant effort and is not expected to affect the current conclusions, it was therefore not undertaken.

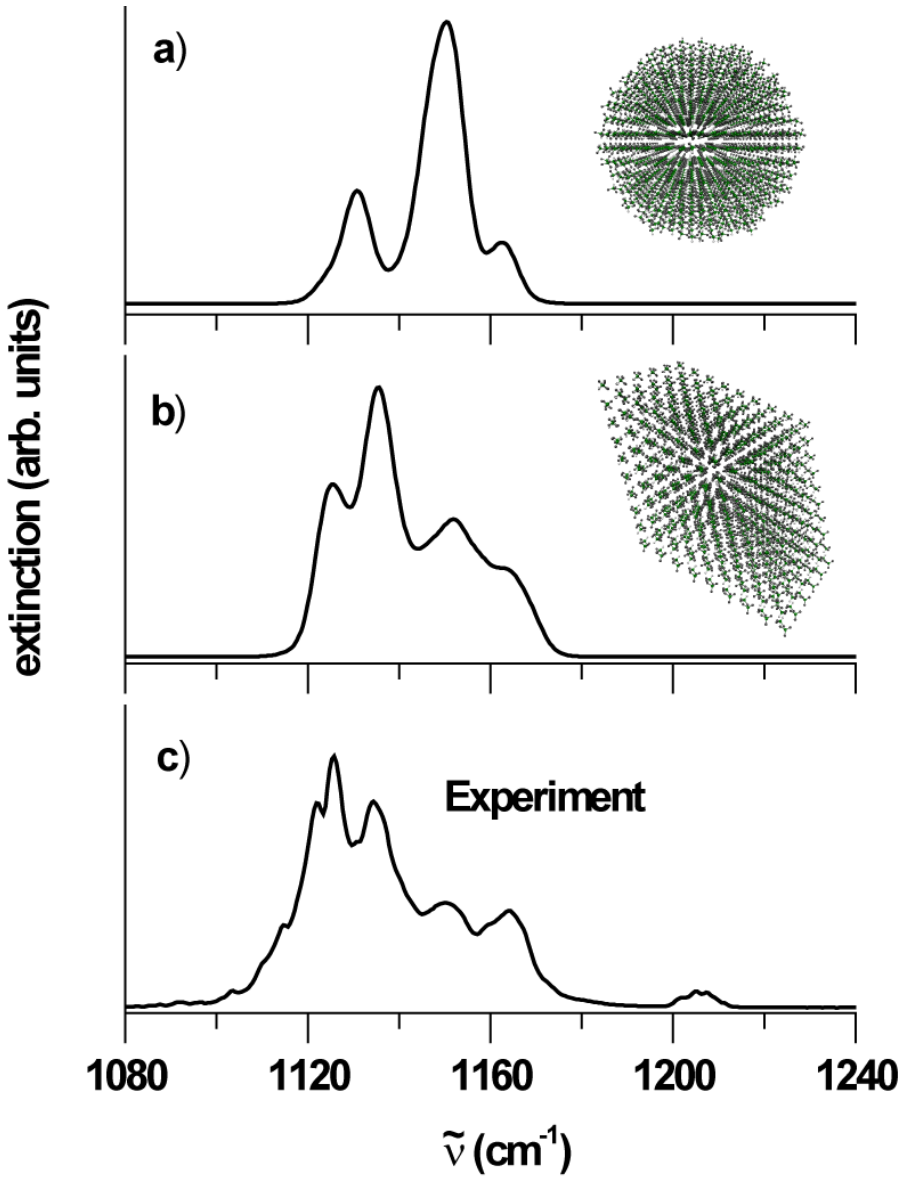

Figure 4.7 Infrared spectra in the region of the ν_5/ν_2 band. a) Vibrational exciton calculation for a crystalline spherical particle. b) Vibrational exciton calculation for a crystalline cube-like particle. c) Experimental infrared spectrum of crystalline cube-like particles (see t = 38 s in Fig. 4.5).

4.5.2 Tracing the Origins of Shape Effects by Exciton Calculations

An added benefit to performing the model calculations with a microscopic model is that it can provide further insights into the molecular origins of the observed band structures. This is done within the quantum mechanical model (eq. 3.13 and 3.14, section 3.1.2) by partitioning up the particles into different regions. By doing so it becomes possible to determine which regions within an aerosol particle (i.e. the molecules from the core versus molecules from the surface) contribute to a certain observed spectral features. Figure 4.8 depicts such an analysis for a spherical crystalline particle (left panel) and a cube-like crystalline particle (right panel). The corresponding infrared spectra are shown on top of the contour plots of the normalized excitation density (see Eq. 3.14) as a function of the distance from the center of the particle. Here, a shell index of 0 corresponds to the center of the particle, increasing linearly up to 10 at the particle's surface. Darker regions indicate strong vibrational excitation and light regions indicate weak vibrational excitations.

Examining the contour plots reveals a different dependence on the origins of excitations for the two different particle shapes. The infrared spectrum of a crystalline sphere (left) is governed by three modes at 1130, 1150 and 1162 cm^{-1} that are delocalized over the whole particle. The two higher wavenumber bands derive most of their intensity from the doubly-degenerate ν_5 transition while the 1130 cm^{-1} band mainly arises from the ν_2 transition. This only conveys the general trend since the two transitions are near resonant and can couple together. Looking at the crystalline cube-like plot we see that the excitation density in the core (shell index 0 to about 6) arises from several modes delocalized over the core, with the density as a smooth function of the wavenumber,

contributing to a weak background in the infrared spectrum. The major structure in the spectrum, however, comes from the highly structured excitation density at or near the surface of the particles (shell index 7 to 10). This is a consequence of the cube-like shape, where the corners represent singularities in the surface curvature. This provides an explanation for features observed in the experimental spectrum in Figures 4.4 (t = 38 s) and 4.7.

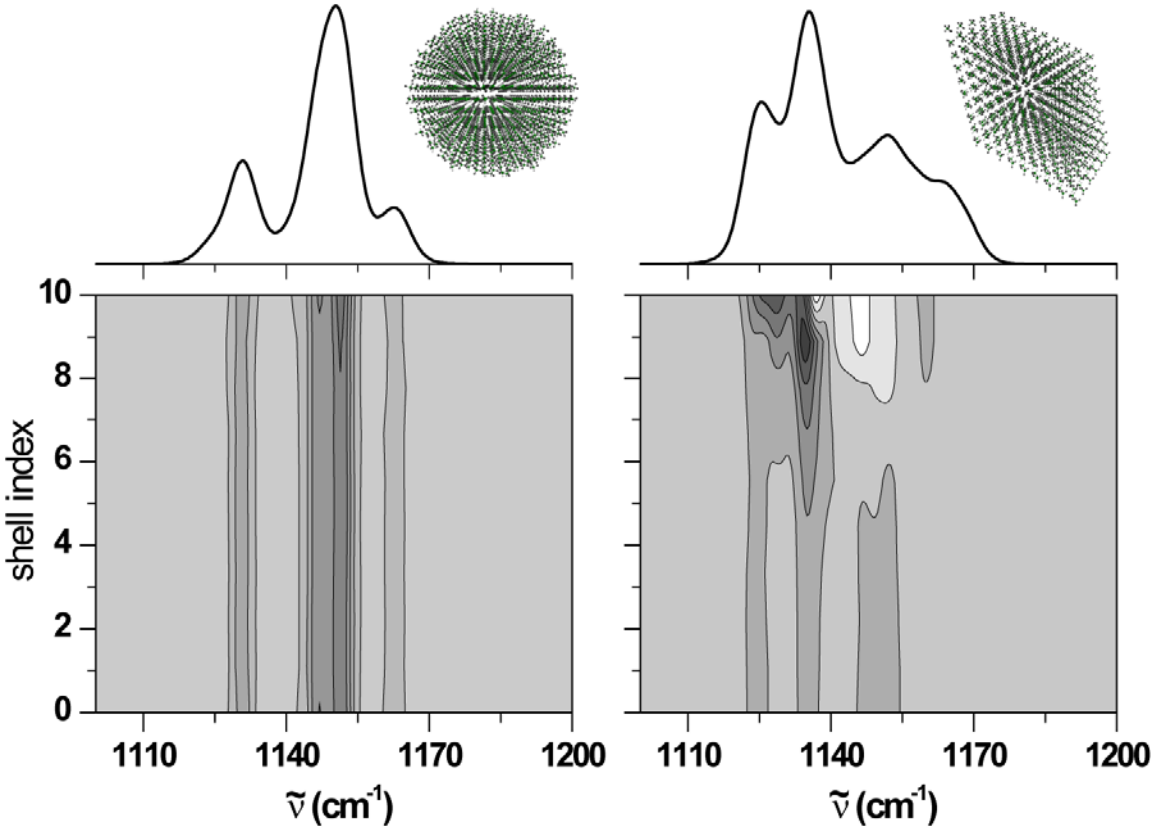

Figure 4.8 Left panels: Crystalline spherical particles. Right panels: Crystalline cube-like particles. Upper panels: Calculated infrared spectra in the region of the ν_5/ν_2 band. Lower panels: Normalized excitation densities as defined in Eq. 3.14.

4.5.3 Identification of Elongated Particles by Exciton Calculations

The sign of a second type of shape change seen in the measured spectra and discussed in section 4.4.3 is the growth of two side bands (arrows in Figure 4.4b) over time. It has been shown in several other studies on aerosol systems [14, 16, 72, 112, 113] that an evolution of side bands indicates the formation of elongated particles from particles initially having closer to equal axis ratio geometries. The previously reported qualitative dependence on experimental conditions matches those found for fluoroform. Namely: i) Elongated particles are formed more quickly at lower bath gas pressures than at higher bath gas pressures. ii) Elongated particles are more easily formed at higher sample gas concentrations than at lower concentrations.

As has been reported [14, 16, 72], the mechanism behind the growth process remains unclear. Both agglomeration and coagulation of cube-like particles as well as the evaporation of small particles and re-condensation onto larger particles are possible explanations. The similar behaviour of fluoroform aerosols as that of previous observations are strong hints that the same shape change is taking place, i.e. the formation of elongated particles from initially mainly cube-like particles. The confirmation of this can be found in Figure 4.9. There the experimental spectra recorded at t = 960 s (thick blue line in trace b) has pronounced side bands compared to the spectra recorded at t = 38 s (thin dotted red line in trace b). This observed trend is reproduced by the calculated spectra in trace a. There the thick line represents a linear combination of cube-like and elongated particles with a:b:c axis ratios of 1:1:9, 1:9:1 and 9:1:1 [49, 102]. The three different axis ratios are equally taken into account in the simulations because it is not known whether growth occurs preferentially along one particular axis. The ratio of

cube-like to elongated particles is 1:1. The thin red dashed line in trace a shows again the exciton calculation for a cube-like particle only. Characteristic side bands arise from elongated particles and are thus more pronounced for higher fractions of elongated particles in the ensemble. As an interesting bit of additional information, the side band at 1157 cm^{-1} appears to be unique to the elongated particles with an axis ratio of 1:9:1. This indicates that growth along the b axis is important as growth along the two other principal axis do not show this feature. While this could point to the possibility that fluoroform particles grow preferentially along the b axis, these simulations cannot conclusively confirm that. This is because of a lack of specific spectral signatures from particles of the other two axis type, making it impossible to rule out their existence. It is worth to mention that the qualitative agreement between experiment and simulation could easily be improved by fitting a broader range of particle shapes (aspect ratios) and ratio of cubic to elongated particles, as well as adjusting the input parameters given in table 4.2. This is however not likely to provide any additional physical insight.

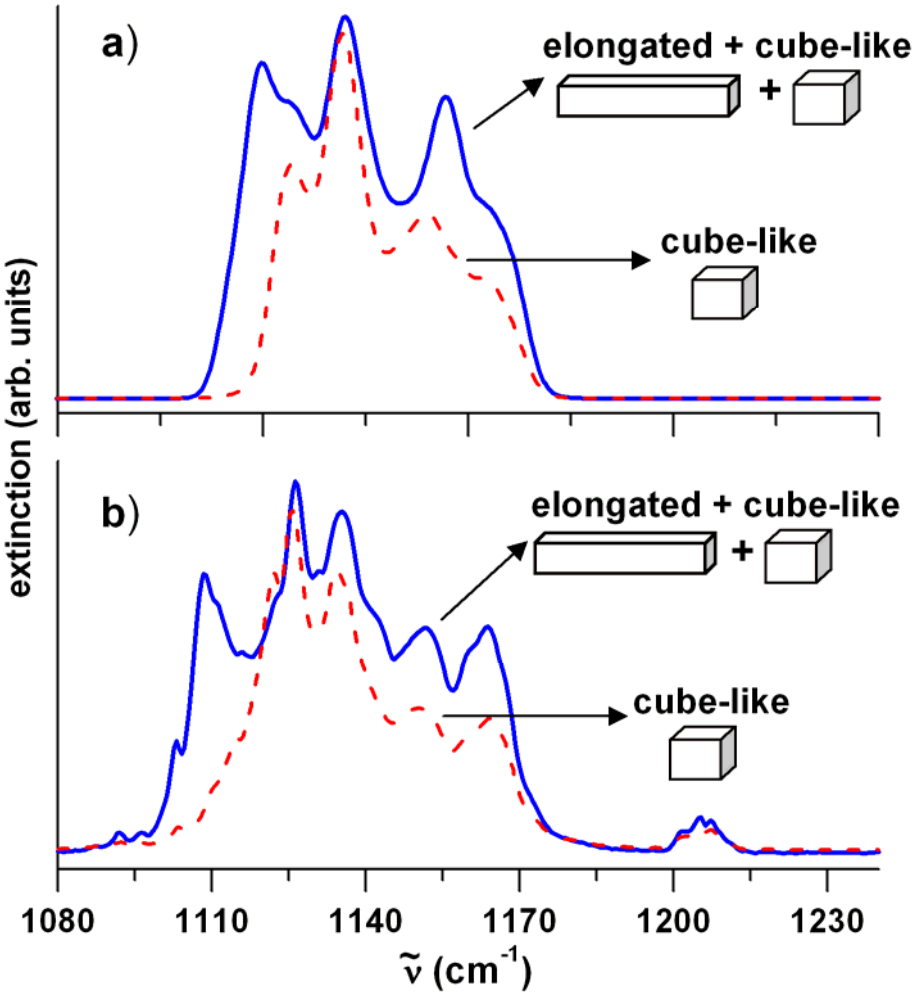

Figure 4.9 Infrared spectra of crystalline particles in the region of the ν_5/ν_2 band. a) Vibrational exciton calculations. Blue thick line: A 1:1 mixture of cube-like and elongated particles. Red dashed line: Pure cube-like particles (see Figure 4.7). b) Experimental spectra. Blue thick line: A mixture of cube-like and elongated particles (estimated 1:1) after 960 s of particle growth. Red dotted line: Cube-like particles immediately after crystallization is complete (see Figure 4.7).

4.6 Summary and Conclusions

The understanding of the dynamic behaviour of aerosols is still in its infancy. The major reason is the complexity of these systems with their many degrees of freedom. By measuring the infrared spectrum of aerosol particle ensembles, many of these processes can be identified and understood. To go beyond a mere speculative interpretation of spectral features it is essential to analyze the experimental data with appropriate model calculations. This is demonstrated using the vibrational exciton model, showing how infrared spectra of molecularly-structured aerosol particles can be understood from molecular properties.

For the example of fluoroform aerosol, the combination of time-dependent infrared spectroscopy and quantitative modeling allows for a detailed understanding of dynamic processes such as crystallization and shape changes of aerosol particles. In the case of homogeneous nucleation (section 4.3) it is concluded based on a kinetic analysis that it is not possible to distinguish between surface and volume nucleation despite claims to the contrary [22, 23]. This is due to inherent experimental shortcomings and inaccurate approximations in the kinetic treatment. The experimentally determined crystallization rates of pure submicron sized fluoroform aerosol droplets were found to be in the range of $J_V = 10^8\text{-}10^{10}$ cm^{-3} s^{-1}, or $J_S = 10^3\text{-}10^5$ cm^{-2} s^{-1} at 78K.

Fluoroform aerosol particles have been shown to exist as supercooled liquid droplets that undergo a phase transition to a monoclinic crystal phase, changing shape from globular droplets to cube-like particles in the process of crystallization. After crystallization they have also been shown to grow in size and become elongated, possibly preferentially in one direction of the crystal axis. A potential practical application is in

the use of fluoroform as a supercritical solvent in processes such as drug micronization by RESS [14, 87], whereby the role of the solvent in the particle formation process can be better understood.

CHAPTER 5

C_2H_6 AEROSOL PARTICLES

5.1 Introduction

The specific interest and motivation to study ethane (C_2H_6) aerosol particles comes primarily from their importance in planetary atmospheres of the outer solar system, in particular on Saturn's moon Titan (see section 1.4). The recent high-profile Cassini-Huygens space mission has provided new information about the nature of Titan and its unique atmosphere, consisting of mainly nitrogen (95-98 %) and methane (1.5-4 %) [37, 38, 40, 41]. Although the temperature on the surface of Titan is only around 94 K, certain similarities have been drawn between Earth, or the early Earth and the conditions on Titan, described in section 1.4 and ref. [37, 38, 40, 41]. Mainly this refers to the presence of a thick atmosphere and dynamic processes that help shape the surface of the moon through precipitation, erosion and geological activity. The primary concern in this regard is the role of methane and ethane aerosol formation in Titans atmosphere, analogous to that of water on Earth. The role of ethane aerosol in Titan's atmosphere is the topic of the next section.

Studying ethane aerosol under controlled conditions in the laboratory allows for the understanding of ethane phase behaviour and helps to clarify the mechanisms of condensation and precipitation under conditions similar to those found on Titan. Well characterized laboratory spectra for different forms and dynamic behaviour of the aerosol particles are vital for their identification through remote sensing. These spectroscopic

studies provide detailed information on the phase behaviour of ethane aerosols at temperatures, total pressures, and saturation ratios relevant to Titan. In addition this information can be of use when exploring ethane's role as a potential interstellar grain molecule, supported by the fact that it has been observed as a volatile compound on comets [114]. It is also worth noting that because of a terrestrial window for observations, the CH bending mode (ν_9 band) of gaseous ethane is used to estimate its abundance and the temperature on Jovian planets [115].

Exciton calculations as performed for fluoroform in the preceding chapter will not yield the same information on the intrinsic particle properties for ethane aerosols. This becomes apparent when the strengths of the transition dipoles for the two substances are compared. The criteria for transition dipole-transition dipole coupling to be the dominant interaction is that the transition dipole needs to be 0.1 D or greater [64, 113]. None of ethane's vibrational modes fulfills this requirement, and thus the information is not present in the infrared spectra.

5.2 The Role of Ethane on Titan

It has been shown that ethane aerosols are potentially a major influence on the weather processes on Titan [32, 38, 116-121]. Widespread permanent ethane clouds, or mist, are likely to be formed above the tropopause (50-80 km above surface) and in the troposphere (0-50 km above surface) in the polar regions [121]. Strong evidence of northern polar ethane clouds at altitudes of 30-50 km were obtained from Cassini's Visual and Infrared Mapping Spectrometer [32]. The aerosol particle sizes have been estimated to be smaller than 3 μm, consistent with microphysical models of Titan's

ethane cloud properties [32, 38, 116-118, 121]. Recent studies also indicate that ethane aerosols could be important condensation nuclei for the formation of methane rain [118-120]. Some scenarios even suggest (although not proven) that methane cloud formation on Titan is limited by the mass of ethane available to form condensation nuclei.

Associated with the condensation and rain formation in the atmosphere is the discussion on ethane reservoirs at the surface of Titan [32, 122, 123]. Recently [42] it has been shown through analysis of Cassini's Radar and IR mapping images that the liquid bodies found in northern polar regions most likely consist of liquid ethane. To account for the lack of a previously hypothesized global hydrocarbon ocean it has been suggested that the ethane produced in Titan's atmosphere gets sequestered in smog particles and deposited on the surface [122].

The presence of ethane on Titan is explained by photochemical reactions of methane in the upper atmosphere [40, 116]. The second most abundant photochemical product (after ethane) is acetylene. As pointed out in section 2.4 (see figure 2.2) acetylene will condense at higher temperatures and lower partial pressures (i.e. higher altitude) than ethane or methane, effectively allowing it to act as a condensation nuclei for those substances when it reaches lower altitudes and temperatures. The abundance of acetylene compared to ethane, however, is a factor of 5-10 less [41, 124, 125], varying with altitude and longitude. The effects of acetylene as condensation nuclei are briefly discussed in section 5.4.

Despite all the observations and speculations listed above, the mechanisms responsible for producing ethane clouds remain poorly understood. This can be traced back to a large extent to the lack of information about ethane aerosol properties under

conditions relevant to Titan's atmosphere, for which no laboratory study of ethane aerosol had been previously reported. Methane and ethane adsorption and heterogeneous nucleation from the gas phase onto supported tholin particles were studied by Curtis *et al.* [119]. This study provides important data on the saturation ratios necessary for ethane condensation to occur. However, there remain major unsolved issues that are crucial for the development of realistic cloud models. Among them is the central question whether supercooled ethane aerosol droplets can form on Titan, analogous to supercooled water clouds in the terrestrial atmosphere [19, 126]. Such clouds were long thought to be impossible to exist but are now known to play an important role in the terrestrial atmosphere. If this is also the case for ethane it would imply that liquid instead of solid condensation nuclei form from gaseous ethane at temperatures where ethane condensation is expected. This is shown to be the case in the following section.

The importance of supercooled droplets then depends on how long they last, i.e. on their freezing kinetics. As has been discussed (section 3.2), freezing can occur homogeneously, or alternatively triggered by the presence of other ice nuclei. To clarify these points, laboratory studies are presented in sections 5.4 and 5.5 dealing with the phase behaviour and kinetics of pure ethane aerosols and ethane aerosols formed in the presence of acetylene ice nuclei under conditions (total pressure, mole fraction, temperature, particle sizes) that mimic the situation in Titan's atmosphere [32, 37, 38, 41, 116, 120, 121, 124, 127-129].

5.3 Experiment

Pure and mixed ethane aerosols were generated by bath gas cooling in a collisional cooling cell (see section 2.2). Time-resolved mid-infrared (500-8000 cm^{-1}) extinction spectra were recorded in situ in the cold cell monitored for 10-15 minutes after particle formation using a rapid-scan Fourier-transform infrared spectrometer, with a resolution of 0.5 cm^{-1}. Prior to aerosol generation the pre-cooled cell (78 K) was filled with He bath gas (pressures 0.1 bar to 1 bar), which after some minutes thermally equilibrated with the cell. In the experiments helium bath gas mimics the role of nitrogen in Titan's atmosphere. In previous investigations it has been found that there is no difference between using N_2 or He as bath gas. Sample gas mixtures consisted of 0.1% to 5% ethane in He. The He/ethane/acetylene mixtures contained up to 1% acetylene. All gas was supplied by Praxair with stated purity of 99.6% or higher. The mole fraction of ethane in the cell varied between 10^{-5} and 10^{-3}. The aerosols investigated had average particle sizes between 0.1 μm to 5 μm as determined from elastic light scattering. The chosen temperature, total pressures, mole fractions, and aerosol particle sizes mimic the conditions expected in Titan's atmosphere [32, 37, 38, 41, 116, 120, 121, 124, 127-129], discussed in section 1.4.

To study the effects of heterogeneous nucleation, the following strategy was used in forming mixed ethane/acetylene aerosols: First, acetylene aerosol particles were formed by injection of acetylene gas mixtures into the cold cell. They then acted as condensation nuclei for ethane. This mimics the situation where acetylene and other photochemical products with lower vapour pressures than ethane condense at higher altitudes in Titan's atmosphere and are transported down to regions where it is cold enough for ethane to

condense, thereby forming condensation nuclei for ethane. Acetylene was chosen because it is one of the most abundant trace species in Titan's atmosphere [38, 41, 124, 127-129] (second most abundant photochemical product of methane). It is therefore a prime candidate for condensation nuclei. Another such candidate would be tholin particles [119, 129], awaiting investigation.

5.4 Analysis of Pure and Mixed Ethane Aerosol Spectra

Recorded infrared spectra of pure ethane aerosols and mixed ethane/acetylene aerosols are shown in Figures 5.1 and 5.2, respectively. Minor contributions from gas phase molecules are barely visible due to the low vapour pressures under those conditions [27, 130, 131]. These spectra provide the first clear experimental evidence that pure ethane aerosol particles as well as mixed ethane/acetylene aerosol particles form under conditions prevalent in Titan's atmosphere. This corroborates the interpretation of recent observations as the formation of ethane clouds in various regions of Titan's atmosphere [32, 121].

A significant change in the IR absorption bands of pure ethane aerosols is observed after their initial formation. Initially broad symmetric bands are found immediately after particle formation (t = 0 s in Figure 5.1). Subsequently a change in the band shapes starts to occur 2-5 minutes after particle formation. The time depends on the experimental conditions (such as pressure and concentration). In Figure 5.1 the time evolution of the ν_9 CH_3 bending mode (panel a), and the ν_8 and ν_6 CH_3 deformation modes (panel b) is shown for pure ethane aerosol. These spectra show clear similarities to the crystallization of fluoroform aerosol (Figure 4.4) presented in section 4.4. Both undergo a transformation from unstructured to structured band shapes and in some cases resulting in very narrow split bands. This is shown to be, in both cases, the result of crystallization of initially supercooled aerosol droplets to a stable low temperature crystal phase (see t = 38 s in Figure 4.5a and t = 874 s in Figures 5.1 and 5.2c). There is, however, an important difference between the crystallization behaviour of ethane versus that of fluoroform. Instead of crystallizing directly to the most stable crystalline phase, ethane undergoes a

phase transitions to an intermediate phase (trace b in Figure 5.2), and finally to the stable, low temperature crystal phase (trace c in Figure 5.2). This is evident by the presence of structured intermediate band shapes in the 818-822 cm^{-1} region of the ν_9 band (arrow in Figure 5.1a). Those differ from the final band shape, which does not absorb in that region. Another indication is the appearance and subsequent disappearance of a side band at 1365 cm^{-1} (arrow in Figure 5.1b). By subtracting any contribution made by the final band shape, it is possible to obtain a pure intermediate spectrum, shown in Figure 5.2b.

With single crystal X-Ray diffraction studies it has been shown that ethane can exist in two stable crystal phases [132-134] as well as a metastable phase [135]. Below 89.9 K ethane adopts the low temperature type II crystal phase, a monoclinic crystal structure with space group $P2_1/n$. Crystalline ethane of type I is an isotropic solid cubic phase with the space group $Im3m$, existing in the very narrow temperature range from 90.33 K to 89.77 K. The two types of crystalline phases observed in the spectra are likely to correspond to those phases and thus two types of phase transitions can take place. The only stable particle phase, however, is the monoclinic crystal phase (phase II), which is also the stable bulk phase at 78 K. All aerosol particles will therefore end up in the phase II crystal phase after completing the phase transitions. Identification of the phase II crystalline structure comes from the infrared spectrum in the region of the υ_9 band with four characteristic peaks at 814 cm^{-1}, 817 cm^{-1}, 824 cm^{-1}, and 825 cm^{-1}, shown in Figure 5.1a, corresponding to values found in the literature [136-138].

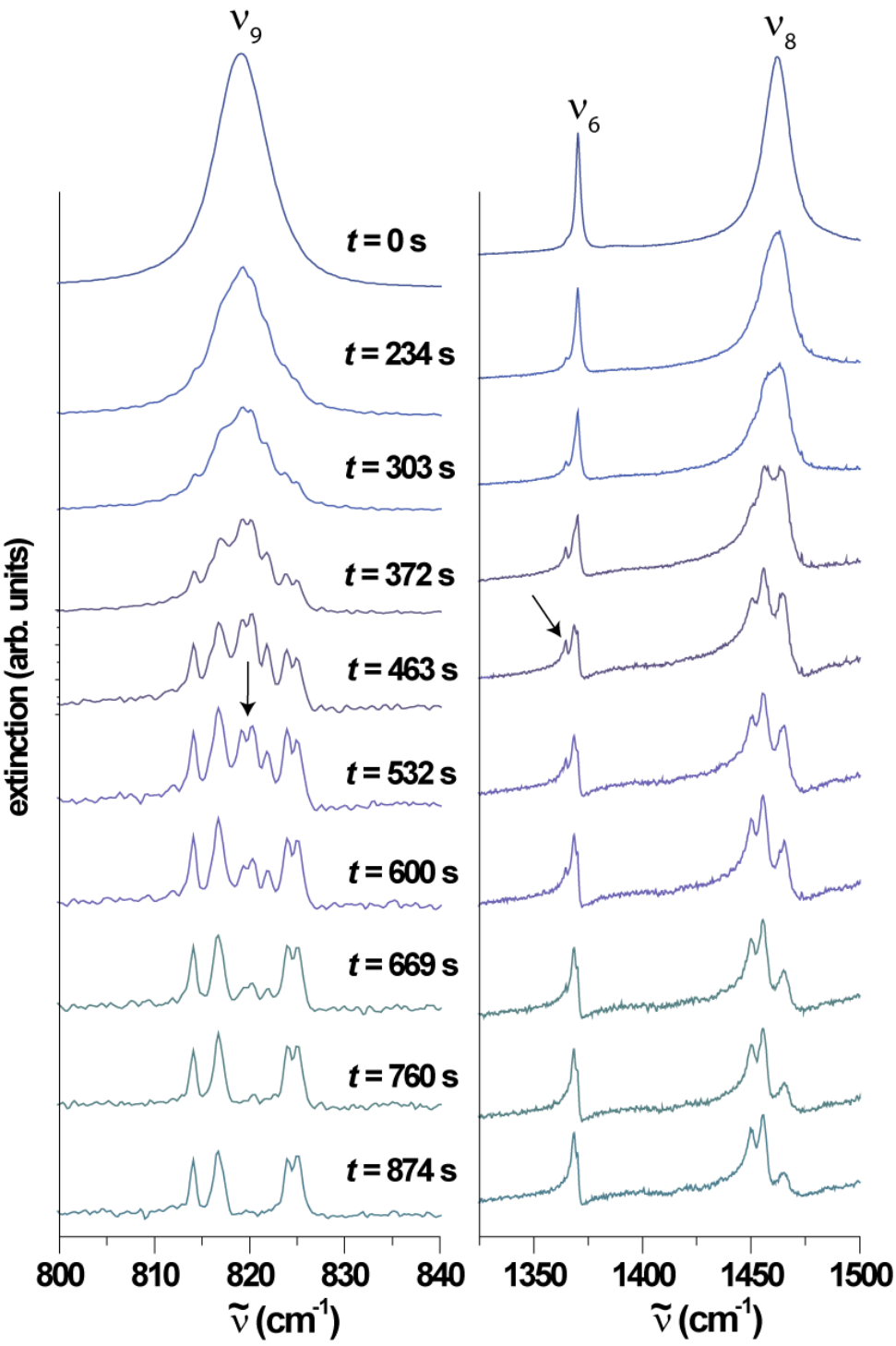

Figure 5.1 Time dependent infrared spectrum of pure C_2H_6 aerosol during crystallization in the region of the ν_9 band (panel a), and the ν_8 and ν_6 bands (panel b). Bands in panel b show signs of increasing elastic scattering due to mean particle size increase. *t* is the time after the particle formation (*t* = 0 s).

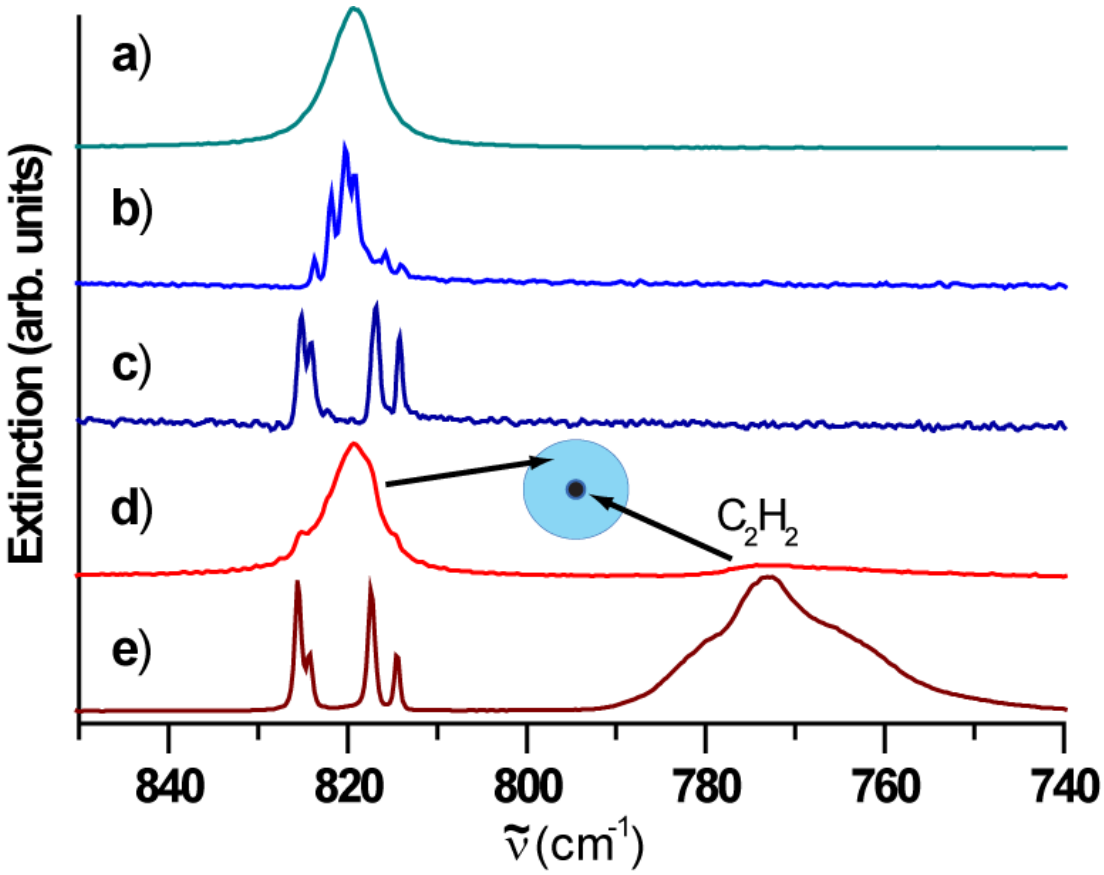

Figure 5.2 Infrared spectra in the region of the υ_9 bending vibration for various ethane aerosols. (a) Pure supercooled ethane droplets immediately after particle formation. (b) Pure ethane particles in crystalline phase I (unstable intermediate phase), observed occasionally during the crystallization process. (c) Pure ethane particles in crystal phase II recorded after crystallization is complete. Phase II is the stable particle phase at 78 K. (d) Droplet with a tiny solid acetylene core and a supercooled liquid ethane shell recorded directly after ethane condensation. The CH-bending vibration of acetylene leads to a weak absorption at 775 cm^{-1}. (e) Particle with a solid acetylene core and a crystalline (phase II) ethane shell observed after crystallization of ethane is complete.

Phase transitions from the supercooled liquid droplets directly to phase II have been observed (no signs of phase I), as well as phase transitions which first form the intermediate crystalline phase (phase I) and in a second step the stable phase II (Fig. 5.1). Which phase transition is favoured depends sensitively on how the crystallization heat is released, and thus on the total pressure and the ethane concentration. For pure ethane, the direct transition from liquid to phase II was more often observed, while heterogeneous crystallizations normally show some signs of contribution from the intermediate phase. The υ_9 band of the pure intermediate phase I is depicted in Fig. 5.2b. This phase most likely corresponds to the crystalline cubic phase described in Ref. [94]. There exists, however, no mid-infrared spectra of this phase for comparison. This is not surprising given the very narrow temperature range in which it exists. However, the appearance of a metastable phase was noted in studies of ethane nucleation on tholin particles [119]. The particular assignment of the phase was however, not specified further. Based solely on the low resolution spectra, it can not be confirmed or ruled out as being the same as the one reported here.

The spectral signs of phase transitions are in all major respects the same for mixed ethane/acetylene aerosols as for pure ethane. The only difference is the higher freezing rate caused by the heterogeneous nucleation of these mixed systems. Fig. 5.2 trace e shows the infrared spectrum of aerosol particles with a solid acetylene core (20 %) and a crystalline ethane shell (80 %) after ethane crystallization is complete. Apart from the varying extent of elastic scattering, there are no unusual size-dependent features observed in the infrared spectra, neither for pure ethane nor for mixed ethane/acetylene particles.

5.5 Evidence for the Formation of Supercooled Ethane Droplets

Immediately after particle formation the infrared bands appear unstructured as depicted in Figure 5.1 (at t = 0 s) and Figure 5.3 (overall spectral range) for pure ethane aerosols, and in Figure 5.2d (region of the υ_9 band) for ethane particles with a tiny solid acetylene core (~1 %) and a thick ethane shell (~99 %). The unstructured, symmetric bands clearly demonstrate a lack of order in the molecular orientations, characteristic of a disordered metastable phase initially being formed. Several pieces of evidence point to this metastable phase being a supercooled liquid. These arguments are similar to those given for fluoroform in section 4.4.1. Firstly, the unstructured infrared bands, as well as the conditions under which the particles are formed are consistent with formation of supercooled liquid droplets. Data available for the vapour pressure over liquid ethane and solid ethane [27, 130, 131] give vapour pressures of $1*10^{-4}$ torr at 78 K over the solid. This is a clear indication that it is possible to form supercooled liquid droplets at 78 K since the ethane partial pressures in the present experiments were higher than extrapolated values over the liquid at this temperature. Further evidence comes from experiments performed above the melting point of ethane (90.3 K) up to temperatures of about 110 K where only liquid droplets can be formed. Exactly the same infrared spectra were found for these "warm" droplets as for the supercooled droplets shown in Fig. 5.3, which confirms the latter's liquid character. The final proof comes from experiments in which ethane droplets were formed first and acetylene ice nuclei were added shortly after. The contact with acetylene ice nuclei led to a near instantaneous crystallization of the ethane particles. This can only be attributed to an initial supercooled liquid ethane phase, freezing heterogeneously.

These experimental results clarify two important issues [25]. First of all, they demonstrate that ethane aerosol particles can indeed be formed under conditions present in Titan's atmosphere. Second, the results prove that under these same conditions the formation of supercooled ethane droplets is possible, similar to the formation of supercooled liquid water droplets in the Earth's atmosphere [19, 126]. This second point is particularly significant as it implies the possibility of forming liquid condensation nuclei, which allows for much more efficient nucleation and condensation processes than solid nuclei [18].

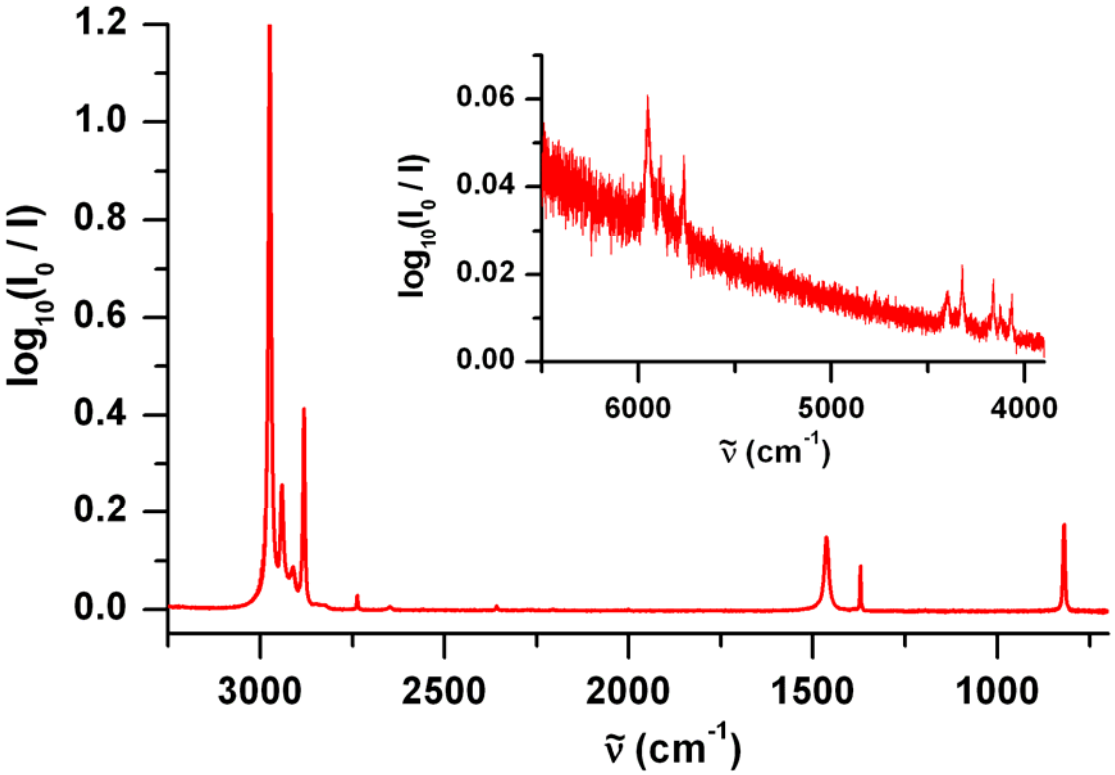

Figure 5.3 Mid-infrared spectrum of pure supercooled ethane droplets recorded immediately after particle formation. The overtone region is shown in the inset. The slanted baseline is due to elastic scattering of the infrared light by the particles.

5.6 Crystallization Kinetics of Ethane Aerosol

The preceding observations on the formation of supercooled ethane droplets raise several questions. How stable are those supercooled liquid droplets and how long do they last, i.e. what are typical freezing rates? What crystal structures can they form and which of them are expected to be relevant and or stable in Titan's atmosphere? To elucidate these points, the crystallization kinetics of ethane aerosols have been investigated by analyzing the time-dependent infrared spectra, depicted in Figure 5.1. The progressive crystallization of supercooled liquid droplets to crystalline aerosol particles is established by analyzing the region of the υ_9 band, presented in section 5.4. This band is very sensitive to the overall molecular environment and thus provides a clear fingerprint of the particle's phase. Note that the strong absorption bands between 2800 cm^{-1} and 3000 cm^{-1} seen in Figure 5.3 are less suitable for this purpose as their appearance is very similar for the crystalline solid phases as for the supercooled droplets shown in Figure 5.3, with only slightly narrower bands (by 2 cm^{-1}) shifted to lower energies (by 2 cm^{-1}) for the crystals. This shows that the CH stretching modes are not very sensitive to the molecular environment.

The crystallization rate constants J_V (if volume nucleation dominates) and J_S (if surface nucleation dominates, see discussion in section 4.3.5 and Ref. [25]) were determined from the analysis of time-dependent infrared spectra. Deconvolution of the spectra following the procedure laid out in section 4.3.1 allowed the fraction of particles P_U that are still unfrozen at time t to be determined. An example is shown in Fig. 5.4. The squares correspond to experimental data points for the transition from the supercooled liquid state to phase II. The crystallization rate constants were determined from a fit (red

dashed line) to the experimental data under the assumption that classical nucleation theory applies. Details of the procedure for the case of fluoroform were given in section 4.3.3 and Ref. [25]. The volume freezing rates found for homogeneous crystallization were $J_V = 10^7$-10^9 $cm^{-3}s^{-1}$ (corresponding surface rates are $J_S = 10^3$-10^5 $cm^{-2}s^{-1}$). Similar rates are observed for transitions where the intermediate phase I was formed. Fits obtained from ethane data on liquid to solid transitions show the same ambiguity when it comes to surface vs. volume crystallization as was found for CHF_3. This further supports the previous conclusion that it is currently not possible to distinguish between the two processes using nucleation rates from particle ensemble measurements performed in cooling cells, due to the inherent uncertainties involved.

A homogeneous freezing rate of $J_V = 10^8$ $cm^{-3}s^{-1}$ means that typical aerosol droplets on Titan with sizes of 1 μm would have freezing times of around 40 min. This is comparable to freezing times of supercooled water droplets in the Earth's atmosphere [19, 126]. Supercooled droplets would therefore not be a transient feature in Titan's ethane clouds, but rather long-lived, at least at sufficiently low abundance of ice nuclei, which can trigger heterogeneous nucleation. Heterogeneous freezing, as is studied here in the presence of solid acetylene condensation nuclei, leads to much higher (several orders of magnitude) freezing rates, depending on the number and size of available nuclei. For the same reasons as put forth for fluoroform in section 4.4.2, the heterogeneous nucleation rates could not be obtained. That is, the size of the acetylene ice nuclei could not be accurately determined due to the lack of elastic light scattering. It is also not at all clear from the current data, whether all or only some acetylene ice nuclei would act as condensation nuclei.

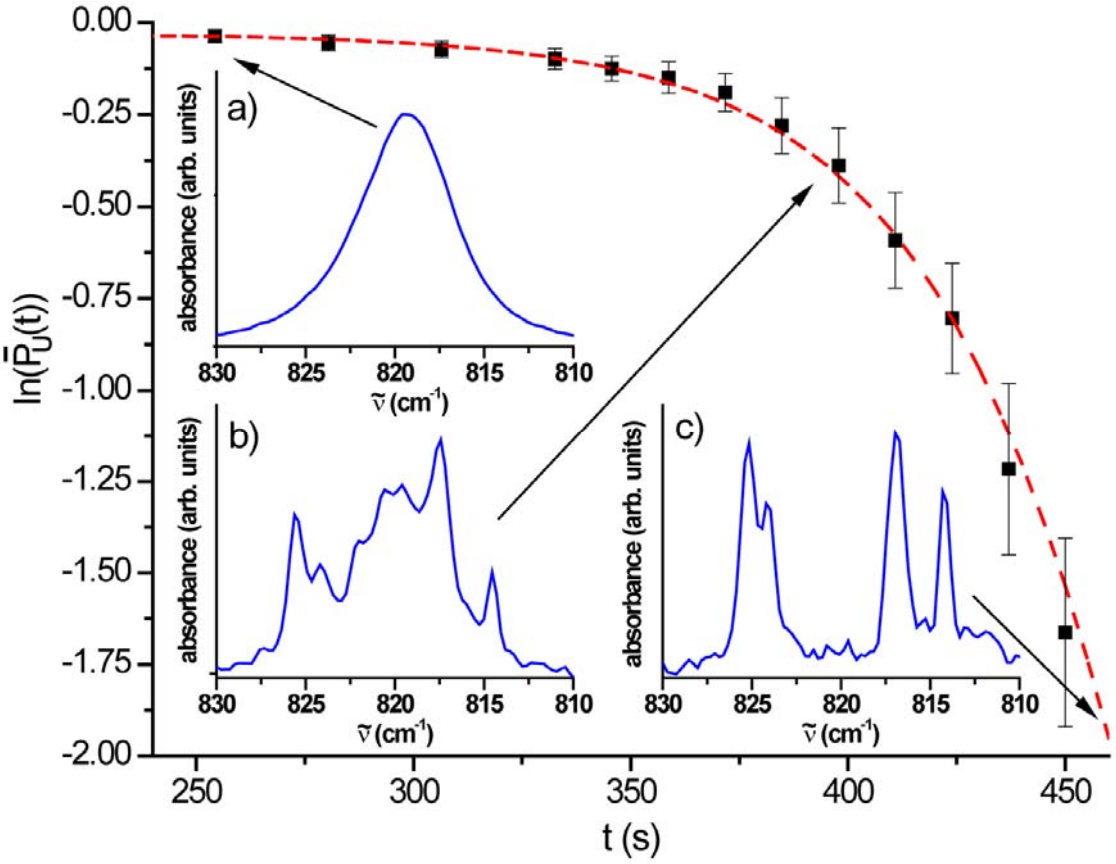

Fig. 5.4 Crystallization kinetics of ethane aerosol particles. Squares: Natural logarithm of the probability P_U that a particle in the ensemble remains unfrozen as a function of time, obtained from a deconvolution of the experimental spectra. Red dashed line: Fit to the experimental data using classical nucleation theory gives $J_V = 10^8$ cm^{-3}s^{-1}. Inserts a) to c): Infrared spectra of ethane aerosol particles during the crystallization from supercooled liquid droplets (trace a) to crystalline particles (trace c).

5.7 Summary and Conclusions

The results presented in section 5.4 illustrate that ethane can indeed condense into aerosol particles under conditions prevalent in Titan's atmosphere. More specifically, the formation of supercooled liquid ethane droplets is possible, demonstrating that efficient nucleation and condensation processes associated with the presence of a liquid rather than a solid phase can occur. The existence of supercooled liquid droplets and liquid condensation nuclei will necessitate revisions to cloud models of Titan, which currently do not take this into account. Based on the homogeneous freezing kinetics that have been determined, supercooled liquid ethane aerosols might have similar impacts in ethane clouds on Titan as supercooled liquid water droplets have in the terrestrial atmosphere. Obtained homogeneous nucleation rates of ethane droplets imply freezing times of minutes up to hours for aerosol particles with sizes below 3 μm at temperatures of 78 K. Supercooled ethane droplets would therefore be a long-lived feature on Titan, at least in regions where the concentration of other ice nuclei is small. In the presence of sufficient amounts of condensation nuclei such as acetylene or tholin particles, ethane aerosols will crystallize rapidly and exist in the same monoclinic crystalline phase as the bulk.

CHAPTER 6

CONCLUSIONS AND FUTURE DIRECTIONS

6.1 Summary and Conclusions

Mid-infrared spectroscopy is a powerful tool to obtain information on the intrinsic particle properties and dynamic processes of molecularly structured aerosol particles. When used in combination with bath gas cooling, *in situ* spectroscopy can be performed on unsupported, sub-micron sized aerosol particles in thermal equilibrium with their surroundings. Analysis of the vibrational dynamics provides in-depth knowledge of processes such as phase transitions and particle shape changes. A true microscopic model such as the vibrational exciton model is required to match observed characteristics in the mid-infrared spectra with the intrinsic particle properties that cause them. With the appropriate investigation tools at hand and the correct theoretical treatment, fundamental questions can be addressed, such as whether particle crystallization initiates from the surface of a particle or within its volume.

Fluoroform aerosol particles, the subject of chapter 4, present a particularly suitable model system. Its distinct spectral features allow us to determine the homogeneous phase transition kinetics, and to monitor the evolution of its particle shape from spherical supercooled droplets to cube-like crystalline particles and eventually to elongated crystalline particles. Approximations widely employed in previous studies of ensemble crystallization kinetics are shown to be unsuitable for distinguishing between surface and volume nucleation. The experimentally obtained crystallization rates do not clearly

favour either one of the nucleation mechanisms due to the inherent experimental uncertainties. This is in contrast to previous reports which claimed the contrary.

In chapter 5, it is for the first time shown that ethane aerosols form under conditions that mimic Titan's atmosphere. An important result is that they are initially formed as supercooled liquid droplets. This also opens up possibilities of alternative and more effective condensation/nucleation mechanisms for the formation of methane clouds. The analysis of their crystallization kinetics reveals that they are likely to be a long lived feature in Titan's atmosphere, analogous to supercooled water in the terrestrial atmosphere. Eventually though, all supercooled ethane droplets that are formed, crystallize to the same stable monoclinic crystalline form as is found for the bulk. This process was shown to be significantly accelerated by the presence of acetylene particles, a potential candidate for condensation nuclei on Titan. During the process of crystallization, it was found that ethane can temporarily exist in a cubic crystalline phase, which is stable only over a narrow temperature range of 0.5 K, making it unlikely to play an important role on Titan. The mid-infrared spectrum of this phase had not been previously reported.

6.2 Remaining Issues and Future Directions

The studies presented in this thesis and in prior publications have revealed detailed information on the properties and dynamic processes of icy aerosol particles from infrared extinction measurements. There are however, a number of questions that remain unanswered. One is the controversial issue of surface versus volume nucleation, addressed in chapter 4. The shortcomings in the way kinetics of particle ensemble measurements were treated in the past have been identified and the correct theoretical treatment provided. However, there remain large uncertainties involved in the experimental determination of the rate constants. For ensemble measurements those can potentially be improved by obtaining more accurate size estimates and by improving the ways of determining the fraction of unfrozen particles. Ideally though, this issue should be addressed by repeated measurements on single, unsupported submicron-sized particles, which is currently not possible. Experimental developments in this direction would have the potential to greatly improve this situation.

Several experiments with two compound systems have been performed within the context of this thesis. In addition to CHF_3/H_2O and C_2H_6/C_2H_2 briefly mentioned in section 4.4.3 and 5.4 respectively, C_2H_6/CO_2 and C_2H_2/CO_2 have also been investigated. Preliminary results of those indicate that CO_2 can act as crystallization nuclei for ethane in much the same way as acetylene does. It is however not as important in the context of Titan's atmosphere. The C_2H_2/CO_2 particles appear to form a co-crystalline phase as is described in references [139, 140]. This sensitively depends on the relative amounts of the two substances. The analysis of these data is still incomplete and further experiments will be required. In particular, heterogeneous nucleation rates where very small ice nuclei

facilitate condensation and induce crystallization are missing from our discussion. As explained in section 4.4.2, this stems from the insufficient accuracy in the determination of the size and number density of the condensation nuclei. In addition, from the present investigations it is also not clear how the condensation nuclei interact with the substance that is condensing on it. Systematic studies should be performed, where condensation nuclei of pre-determined size are varied in concentration and size to determine its influence on the crystallization kinetics. Different types of condensation nuclei should also be explored in order to identify what determines their effectiveness.

The growth mechanism responsible for the observed increase in particle sizes with time (Table 4.1) still remains to be explained. Currently we are confined to speculations as to whether gas evaporates from small particles and re-condenses on larger ones or a more direct interaction takes place, whereby particles collide and coagulate. It is also entirely possible that both processes are taking place and that their importance depends on the experimental conditions. If further evidence can be found for a preferential growth of particles along one particular axis (suggested in section 4.5.3) it would imply a particle growth mechanism of evaporation and recondensation. It would appear unlikely that this could occur by random collisions of particles. However, a change in particle shape towards elongated particles could possibly result from random collisions of mainly globular or cube-like particles. The possibility of growth by accumulation of gas particles also seems possible, although often no gas-phase spectral lines are observed during particle growth.

Despite great stride in our knowledge of Titan as a result of the Cassini-Huygens mission, its aerosols and their role in the atmosphere remains unclear. With continuing

analysis of the measurement data from Cassini-Huygens, more questions will be clarified, but there will still be a need for laboratory studies, where the properties of the aerosols are explored under controlled conditions. Most important in this respect are studies on methane and its photochemical products. Further clarifications of the processes of methane condensation in the presence of various solid and liquid condensation nuclei is vital in determining if and how methane clouds form, what their likely makeup is, and how they can evolve.

A major constituent of aerosols in Titan's atmosphere that has not been covered in this thesis are tholin particles that make up the haze layer which obscures the surface of the moon to visible light. In order to perform studies on substances of this kind they have to be produced in a laboratory. This would require modifying the current experimental setup or setting up a new experiment whereby the tholin particles are produced, either by electrical discharge or photo-ionization of the gas phase species present in Titan's atmosphere.

REFERENCES

[1] J. H. Seinfeld, and S. N. Pandis, *Atmospheric Chemistry and Physics: From air pollution and climate change* (Wiley & Sons, New York, 1998).

[2] B. J. Finlayson-Pitts, and J. N. Pitts, *Chemistry of the Upper and Lower Atmosphere* (Academic Press, San Diego, 2000).

[3] R. Courtin, Space Sci. Rev. **116**, 185 (2005).

[4] S. G. Gibbard *et al.*, Icarus **166**, 359 (2003).

[5] P. Ehrenfreund, and S. B. Charnley, Annu. Rev. Astron. Astrophys. **38**, 427 (2000).

[6] D. M. Murphy *et al.*, Nature **392**, 62 (1998).

[7] E. Herbst, in *Highlights of Astronomy, Vol 12* (Astronomical Soc Pacific, San Francisco, 2002), pp. 55.

[8] A. D. Kappos *et al.*, Int. J. Hyg. Environ. Health. **207**, 399 (2004).

[9] K. Willeke, and P. Baron, *Aerosol Measurement: Principles, Techniques and Applications* (John Wiley and Sons, New York, 2001).

[10] T. L. Rogers, K. P. Johnston, and R. O. Williams, Drug Dev. Ind. Pharm. **27**, 1003 (2001).

[11] J. P. Reid *et al.*, Int. Rev. Phys. Chem. **26**, 139 (2007).

[12] *Faraday Discussion 137: The Spectroscopy and Dynamics of Microparticles* (2008).

[13] T. E. Gough, and T. Wang, J. Chem. Phys. **105**, 4899 (1996).

[14] G. Firanescu *et al.*, Phys. Chem. Chem. Phys. **8**, 4149 (2006).

[15] G. Firanescu, D. Luckhaus, and R. Signorell, J. Chem. Phys. **125**, 13 (2006).

[16] G. Firanescu, D. Luckhaus, and R. Signorell, J. Chem. Phys. **128**, 9 (2008).

[17] O. F. Sigurbjornsson, G. Firanescu, and R. Signorell, Annu. Rev. Phys. Chem. **60**, 127 (2009).

[18] L. Guez *et al.*, Planet. Space Sci. **45**, 611 (1997).

[19] D. Rosenfeld, and W. L. Woodley, Nature **405**, 440 (2000).

[20] A. Tabazadeh, Atmos. Chem. Phys. **3**, 863 (2003).

[21] A. Tabazadeh, J. Phys. Chem. A **111**, 1374 (2007).

[22] A. Tabazadeh *et al.*, J. Phys. Chem. A **106**, 10238 (2002).

[23] A. Tabazadeh, Y. S. Djikaev, and H. Reiss, Proc. Nat. Acad. Sci. U.S.A. **99**, 15873 (2002).

[24] Y. S. Djikaev *et al.*, J. Phys. Chem. A **106**, 10247 (2002).

[25] O. F. Sigurbjornsson, and R. Signorell, Phys. Rev. E **77**, 051601 (2008).

[26] B. A. Smith *et al.*, Science **246**, 1422 (1989).

[27] J. I. Moses, M. Allen, and Y. L. Yung, Icarus **99**, 318 (1992).

[28] M. J. Frisch *et al.*, in *Gaussian 03* (Gaussian, Inc., Wallingford CT, 2004).

[29] T. Encrenaz *et al.*, Astron. Astrophys. **358**, L83 (2000).

[30] C. C. Porco *et al.*, Nature **434**, 159 (2005).

[31] R. de Kok *et al.*, Icarus **191**, 223 (2007).

[32] C. A. Griffith *et al.*, Science **313**, 1620 (2006).

[33] M. H. Wong *et al.*, Planet. Space Sci. **52**, 385 (2004).

[34] F. W. Taylor *et al.*, Planet. Space Sci. **46**, 1315 (1998).

[35] G. F. Lindal *et al.*, J. Geophys. Res-Space Phys. **92**, 14987 (1987).

[36] T. Encrenaz, C. R. Acad. Sci. Ser. IV-Phys. Astrophys. **1**, 1245 (2000).

[37] M. Fulchignoni *et al.*, Nature **438**, 785 (2005).

[38] M. G. Tomasko *et al.*, Nature **438**, 765 (2005).

[39] B. Ragent *et al.*, Science **272**, 854 (1996).

[40] J. I. Lunine, and S. K. Atreya, Nature Geoscience **1**, 159 (2008).

[41] H. B. Niemann *et al.*, Nature **438**, 779 (2005).

[42] R. H. Brown *et al.*, Nature **454**, 607 (2008).

[43] P. P. Lavvas, A. Coustenis, and I. M. Vardavas, Planet. Space Sci. **56**, 67 (2008).

[44] S. J. Kim, L. M. Trafton, and T. R. Geballe, Astrophys. J. Lett. **679**, L53 (2008).

[45] C. Sagan, and B. N. Khare, Nature **277**, 102 (1979).

[46] C. P. McKay *et al.*, Planet. Space Sci. **49**, 79 (2001).

[47] G. D. McDonald *et al.*, Icarus **108**, 137 (1994).

[48] B. N. Khare *et al.*, Icarus **160**, 172 (2002).

[49] O. F. Sigurbjornsson, G. Firanescu, and R. Signorell, Phys. Chem. Chem. Phys., DOI: 10.1039/b813756k (2008).

[50] O. F. Sigurbjornsson, and R. Signorell, Phys. Chem. Chem. Phys. **10**, 6211 (2008).

[51] M. Herman *et al.*, Int. Rev. Phys. Chem. **19**, 277 (2000).

[52] R. Disselkamp, and G. E. Ewing, J. Chem. Phys. **99**, 2439 (1993).

[53] M. L. Clapp, and R. E. Miller, Icarus **105**, 529 (1993).

[54] T. Dunder, and R. E. Miller, J. Chem. Phys. **93**, 3693 (1990).

[55] B. Rowland, N. S. Kadagathur, and J. P. Devlin, J. Chem. Phys. **102**, 13 (1995).

[56] L. Delzeit *et al.*, J. Phys. Chem. **100**, 10076 (1996).

[57] S. Bauerecker *et al.*, Rev. Sci. Instrum. **72**, 3946 (2001).

[58] M. K. Kunzmann *et al.*, Phys. Chem. Chem. Phys. **3**, 3742 (2001).

[59] *CRC Handbook of Chemistry and Physics* (CRC Press, Cleveland, Ohio 1997).

[60] J. U. White, J. Opt. Soc. Am. **32**, 285 (1947).

[61] J. A. Barnes, and T. E. Gough, J. Chem. Phys. **86**, 6012 (1987).

[62] T. A. Beu, C. Steinbach, and U. Buck, J. Chem. Phys. **117**, 3149 (2002).

[63] G. Cardini, V. Schettino, and M. L. Klein, J. Chem. Phys. **90**, 4441 (1989).

[64] R. Signorell, J. Chem. Phys. **118**, 2707 (2003).

[65] J. C. Maxwell, Philos. Trans. R. Soc. London **155**, 459 (1865).

[66] C. F. Bohren, and D. R. Huffman, *Absorption and Scattering of Light by Small Particles* (Wiley-Interscience, New York, 1998).

[67] H. C. v. d. Hulst, *Light Scattering by Small Particles.* (Dover Publications, New York, 1981).

[68] J. P. Reid, and L. Mitchem, Annu. Rev. Phys. Chem. **57**, 245 (2006).

[69] M. A. Yurkin, and A. G. Hoekstra, J. Quant. Spectrosc. Radiat. Transfer **106**, 558 (2007).

[70] E. M. Purcell, and C. R. Pennypacker, Astrophys. J. **186**, 705 (1973).

[71] P. Yang *et al.*, Appl. Optics **39**, 3727 (2000).

[72] R. Signorell *et al.*, J. Phys. Chem. A **110**, 2890 (2006).

[73] D. Fox, and R. M. Hexter, J. Chem. Phys. **41**, 1125 (1964).

[74] R. M. Hexter, J. Chem. Phys. **33**, 1833 (1960).

[75] M. Volmer, and A. Weber, Z. Phys. Chem. (Leipzig) **119** (1926).

[76] L. Farkas, Z. Phys. Chem. (Leipzig) **125** (1927).

[77] R. Becker, and W. Döring, Annalen der Physik **416**, 719 (1935).

[78] D. Turnbull, and J. C. Fisher, J. Chem. Phys. **17**, 71 (1949).

[79] K. F. Kelton, Solid State Physics-Advances in Research and Applications **45**, 75 (1991).

[80] D. Kashchiev, *Nucleation. Basic Theory with Applications* (Butterworth-Heinemann, Oxford, 2000).

[81] J. W. P. Schmelzer, *Nucleation Theory and Applications* (Wiley-VCH, Weinheim, 2005).

[82] J. W. Mullin, *Crystallization* (Butterworth-Heinemann, Oxford; Boston, 2001).

[83] A. G. Walton, in *Nucleation*, edited by A. C. Zettlemoyer (M. Dekker:, New York, 1969), pp. 225.

[84] M. T. Parsons, in *Department of Chemistry* (University of British Columbia, Vancouver, 2006).

[85] J. L. Katz, Pure Appl. Chem. **64**, 1661 (1992).

[86] D. Duft, and T. Leisner, Atmos. Chem. Phys. **4**, 1997 (2004).

[87] A. Bonnamy *et al.*, Rev. Sci. Instrum. **76**, 8 (2005).

[88] J. E. Kay *et al.*, Atmos. Chem. Phys. **3**, 1439 (2003).

[89] D. A. Knopf, J. Phys. Chem. A **110**, 5745 (2006).

[90] O. Stetzer *et al.*, Atmos. Chem. Phys. **6**, 3023 (2006).

[91] P. Stockel *et al.*, J. Phys. Chem. A **109**, 2540 (2005).

[92] G. W. Turner, and L. S. Bartell, J. Phys. Chem. A **109**, 6877 (2005).

[93] A. K. Bertram, and J. J. Sloan, J. Geophys. Res.-Atmos. **103**, 3553 (1998).

[94] R. S. Disselkamp *et al.*, J. Phys. Chem. **100**, 9127 (1996).

[95] J. F. Huang, and L. S. Bartell, J. Phys. Chem. **99**, 3924 (1995).

[96] A. J. Prenni *et al.*, J. Geophys. Res.-Atmos. **103**, 28439 (1998).

[97] D. Salcedo, L. T. Molina, and M. J. Molina, J. Phys. Chem. A **105**, 1433 (2001).

[98] S. E. Wood, M. B. Baker, and B. D. Swanson, Rev. Sci. Instrum. **73**, 3988 (2002).

[99] E. H. G. Backus *et al.*, Phys. Rev. Lett. **92** (2004).

[100] J. F. Huang, and L. S. Bartell, J. Phys. Chem. **98**, 4543 (1994).

[101] K. A. Mort *et al.*, Mol. Phys. **90**, 415 (1997).

[102] B. H. Torrie, O. S. Binbrek, and B. M. Powell, Mol. Phys. **87**, 1007 (1996).

[103] W. C. Hinds, *Aersosol Technology: properties, behavior and measurement of airborn particles* (Wiley, New York, 1999).

[104] S. M. Melikova *et al.*, Chem. Phys. Lett. **352**, 301 (2002).

[105] S. G. Ramesh, and E. L. Sibert, Mol. Phys. **103**, 149 (2005).

[106] M. Horsch *et al.*, J. Chem. Phys. **128**, 9 (2008).

[107] W. Ostwald, Z. Phys. Chem. **22**, 289 (1897).

[108] J. Schmelzer, J. Moller, and I. Gutzow, Z. Phys. Chemie-Int. J. Res. Phys. Chem. Chem. Phys. **204**, 171 (1998).

[109] H. W. Xiang, J. Phys. Chem. Ref. Data **30**, 1161 (2001).

[110] F. Baas, and K. D. Van den Hout, Physica A **95**, 597 (1979).

[111] T. Hahn, *International Tables for Crystallography* (Kluwer, Dordrecht, 1983).

[112] M. Jetzki, A. Bonnamy, and R. Signorell, J. Chem. Phys. **120**, 11775 (2004).

[113] R. Signorell, and M. K. Kunzmann, Chem. Phys. Lett. **371**, 260 (2003).

[114] N. Dello Russo *et al.*, Icarus **184**, 255 (2006).

[115] J. V. Auwera, N. Moazzen-Ahmadi, and J. M. Flaud, Astrophys. J. **662**, 750 (2007).

[116] S. K. Atreya *et al.*, Planet. Space Sci. **54**, 1177 (2006).

[117] E. L. Barth, and O. B. Toon, Icarus **162**, 94 (2003).

[118] E. L. Barth, and O. B. Toon, Icarus **182**, 230 (2006).

[119] D. B. Curtis *et al.*, Icarus **195**, 792 (2008).

[120] S. D. B. Graves *et al.*, Planet. Space Sci. **56**, 346 (2008).

[121] P. Rannou *et al.*, Science **311**, 201 (2006).

[122] D. M. Hunten, Nature **443**, 669 (2006).

[123] O. Mousis, and B. Schmitt, Astrophys. J. Lett. **677**, L67 (2008).

[124] S. Vinatier *et al.*, Icarus **188**, 120 (2007).

[125] A. Coustenis *et al.*, Icarus **189**, 35 (2007).

[126] H. R. Pruppacher, and J. D. Klett, *Microphysics of Clouds and Precipitation,* (Kluwer Academic, Norwell, Massachusetts, 1997).

[127] M. C. Liang, Y. L. Yung, and D. E. Shemansky, Astrophys. J. **661**, L199 (2007).

[128] N. A. Teanby *et al.*, Icarus **193**, 595 (2008).

[129] J. H. Waite *et al.*, Science **316**, 870 (2007).

[130] M. Funke, R. Kleinrahm, and W. Wagner, J. Chem. Thermodyn. **34**, 2017 (2002).

[131] R. N. Nelson, and J. E. Allen, Bull. Am. Astron. Soc. **32** (2000).

[132] M. G. Wisnosky *et al.*, J. Chem. Phys. **79**, 3505 (1983).

[133] G. J. H. van Nes, and A. Vos, Acta Crystallographica Section B-Structural Science **34**, 1947 (1978).

[134] D. F. Eggers, J. Phys. Chem. **79**, 2116 (1975).

[135] M. G. Wisnosky *et al.*, J. Chem. Phys. **79**, 3513 (1983).

[136] A. J. Rest, R. Warren, and S. C. Murray, Appl. Spectrosc. **50**, 517 (1996).

[137] M. G. Wisnosky *et al.*, J. Chem. Phys. **79**, 3505 (1983).

[138] S. B. Tejada, and D. F. Eggers, Spectrochim. Acta, Part A **32**, 1557 (1976).

[139] T. E. Gough, and T. Wang, J. Chem. Phys. **102**, 3932 (1995).

[140] T. E. Gough, and T. E. Rowat, J. Chem. Phys. **109**, 6809 (1998).